ACS NANO

www.acsnano.org

ARTICLE

Highly Conductive, Adhesive and Biocompatible Hydrogel for Closed-Loop Neuromodulation in Nerve Regeneration

Tianfei Chu,[#] Yuanjie Xiao,[#] Huiting Lai, Liangjing Shi, Yin Cheng, Jing Sun, Zhen Pang, Shihui Cheng, Kunkun Zhao, Zhengrun Gao,* and Ranran Wang*

Cite This: *ACS Nano* 2025, 19, 18729−18746

Read Online

ACCESS | Metrics & More | Article Recommendations | Supporting Information

ABSTRACT: **Developing conductive hydrogels has led to significant advancements in bioelectronics, especially in the realms of neural interfacing and neuromodulation. Despite this progress, the synthesis of hydrogels that simultaneously exhibit superior mechanical stretchability, robust bioadhesion, and high conductivity remains a significant challenge. Traditional approaches often resort to high filler concentrations to achieve adequate electrical conductivity, which detrimentally affects the hydrogel's mechanical integrity and biocompatibility. In this study, we present a multifunctional conductive hydrogel, designated as PAACP, which is engineered from a polyacrylamide−poly(acrylic acid) (PAM−PAA) matrix and enhanced with polydopamine-modified carbon nanotubes (CNT-PDA). This composition ensures an exceptional conductivity of 9.52 S/m with a remarkably low carbon nanotube content of merely 0.33 wt %. The hydrogel exhibits excellent mechanical properties, including low tensile modulus (∼100 kPa), high stretchability (∼1000%), and high toughness (7.33 kJ m^{-2}). Moreover, the synergistic action of catechol and NHS ester functional groups provides strong tissue adhesive strength (107.14 kPa), ensuring stable bioelectronic−neural interfaces. As a cuff electrode, it enables suture-free implantation and bidirectional electrical communication with the sciatic nerve, which is essential for neuromodulation. Leveraging these capabilities, our hydrogel is integrated into a closed-loop system for sciatic nerve repair, significantly enhancing real-time feedback driven nerve regeneration and accelerating functional recovery. This work offers a strategy for dynamic, personalized neuromodulation in nerve repair and clinical applications.**

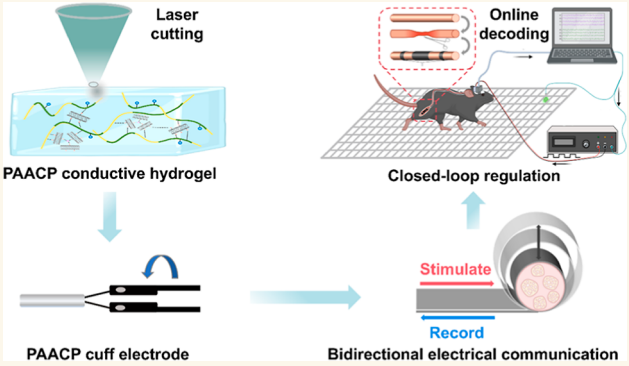

KEYWORDS: *bioelectronics, conductive hydrogel, electrophysiological recording, neuromodulation, closed-loop system*

INTRODUCTION

The peripheral nervous system (PNS) plays a crucial role in mediating communication between the central nervous system (CNS) and various motor and sensory nerve terminals.[1,2] As such, recording and stimulating the PNS provide an opportunity to monitor and regulate the functions of corresponding organs.[3]

A closed-loop neuroregulation system modulates neural regulation parameters by combining continuous physiological monitoring and feedback, offering a dynamic and real-time treatment approach for diseases with fluctuating symptoms. Electrical stimulation therapies targeting the PNS have demonstrated significant therapeutic potential in the treatment of various diseases.[4−6] By integrating closed-loop neuroregulation systems and continuously adjusting based on real-time data, more effective and personalized care can be provided for chronic and complex diseases such as Parkinson's disease, epilepsy, and neuropathic pain.[7,8]

Biointerface electrodes, such as cuff electrodes, which possess both recording and stimulating capabilities, are key components for achieving closed-loop neuroregulation.[9,10] However, traditional commercial cuff electrodes are typically made from flexible silicone rubber substrates and rigid materials like metals. The significant mechanical mismatch between the rigid cuff and the soft neural tissue generates high pressure, which can trigger

Received: February 24, 2025
Revised: April 30, 2025
Accepted: April 30, 2025
Published: May 8, 2025

https://doi.org/10.1021/acsnano.5c03336
ACS Nano 2025, 19, 18729−18746

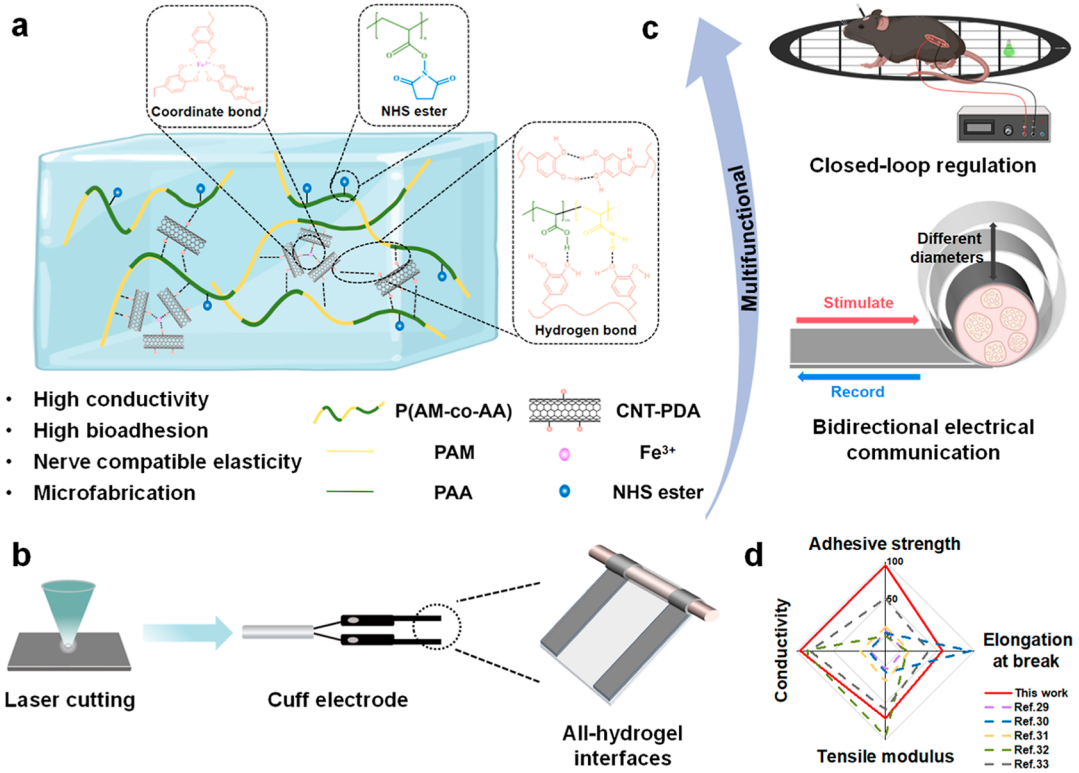

Figure 1. Schematic illustration of PAACP conductive hydrogel for bidirectional electrical communication and closed-loop regulation. (a) Schematic of the PAACP conductive hydrogel structure. (b) Schematic of PAACP conductive hydrogel laser cutting fabrication. (c) Applications of PAACP conductive hydrogel. (d) Comparison of PAACP conductive hydrogel with other conductive hydrogels in terms of conductivity, adhesive strength, tensile modulus, and elongation at break.

severe inflammatory responses and fibrosis. This fibrotic encapsulation eventually blocks electrical communication at the nerve interface, resulting in the failure of the implanted bioelectronic devices.[11] At the same time, while much attention has been given to the stimulating capabilities of commercial cuff electrodes for direct intervention in neural function, their recording performance is often relatively poor. Over the past decade, significant efforts have been devoted to developing the next generation of implantable bioelectronics based on soft electronic technologies, with the aim of reducing the mechanical mismatch associated with chronic implants and mitigating adverse immune responses.[12] While significant progress has been made in fabricating soft and compliant bioelectronic devices using flexible substrates like polydimethylsiloxane (PDMS) or shape-memory polymers, seamless integration of cuff electrodes with peripheral nerves remains a significant challenge. Common strategies for attaching flexible cuff electrodes to peripheral nerves include self-locking cuff electrodes, helically wrapped neural ribbon cuff electrodes, or the design of ultrathin electrodes that physically adhere to the nerve epineurium *via* van der Waals forces.[13−15] However, the weak physical interactions between the neural electrode and the nerve tissue often fail to ensure the close and stable contact necessary for reliable long-term electrical communication at the bioelectronic−neural interface.

In recent years, conductive hydrogels have attracted widespread attention in the field of flexible wearable electronics[16−22] due to their superior electrochemical properties and outstanding mechanical flexibility.[23] These hydrogels, typically composed of hydrogel matrices and conductive fillers, effectively minimize the mechanical mismatch at the neural electrode-tissue interface, thereby minimizing the foreign body response associated with electrode implantation and enhancing the stability of bioelectronic−neural interface electrical communication. As such, conductive hydrogels are considered ideal materials for neural interfaces.[24] Ko *et al.* employed laser-induced phase separation (LIPSA) to fabricate high-stability, highly conductive PEDOT:PSS hydrogels, which were used to create microelectrode arrays for stable and reusable electrophysiological signal recording from rat brains and hearts.[25] Zhao *et al.* developed a bicontinuous conducting polymer hydrogel using PEDOT:PSS as the electrical phase and hydrophilic polyurethane as the mechanical phase, enabling long-term electrophysiological recording and stimulation of various organs in rat models.[26] Nishizawa *et al.* developed a self-closing organic cuff electrode by embedding soft PEDOT−PU electrodes into a PVA hydrogel bilayer, enabling effective vagus nerve stimulation in pigs without causing nerve damage.[6]

However, even though these promising results, several challenges remain. The content of conductive fillers is often excessively high (*e.g.*, >20%),[25,26] and many of the additives used in the fabrication of PEDOT:PSS hydrogels are cytotoxic, requiring several days for detoxification.[27] While current processing methods have improved the biocompatibility of PEDOT:PSS hydrogels, achieving good electrical conductivity at lower filler contents is still a goal. Furthermore, current all hydrogel-based cuff electrodes typically rely on stress differences across bilayer interfaces or additional adhesive layers to facilitate the implantation of the cuff electrode onto the nerve,[6,26,28] as the conductive layer itself generally lacks adhesion.

We envision an ideal hydrogel-based flexible neural electrode that achieves good electrical performance with low conductive

https://doi.org/10.1021/acsnano.5c03336
ACS Nano 2025, 19, 18729−18746

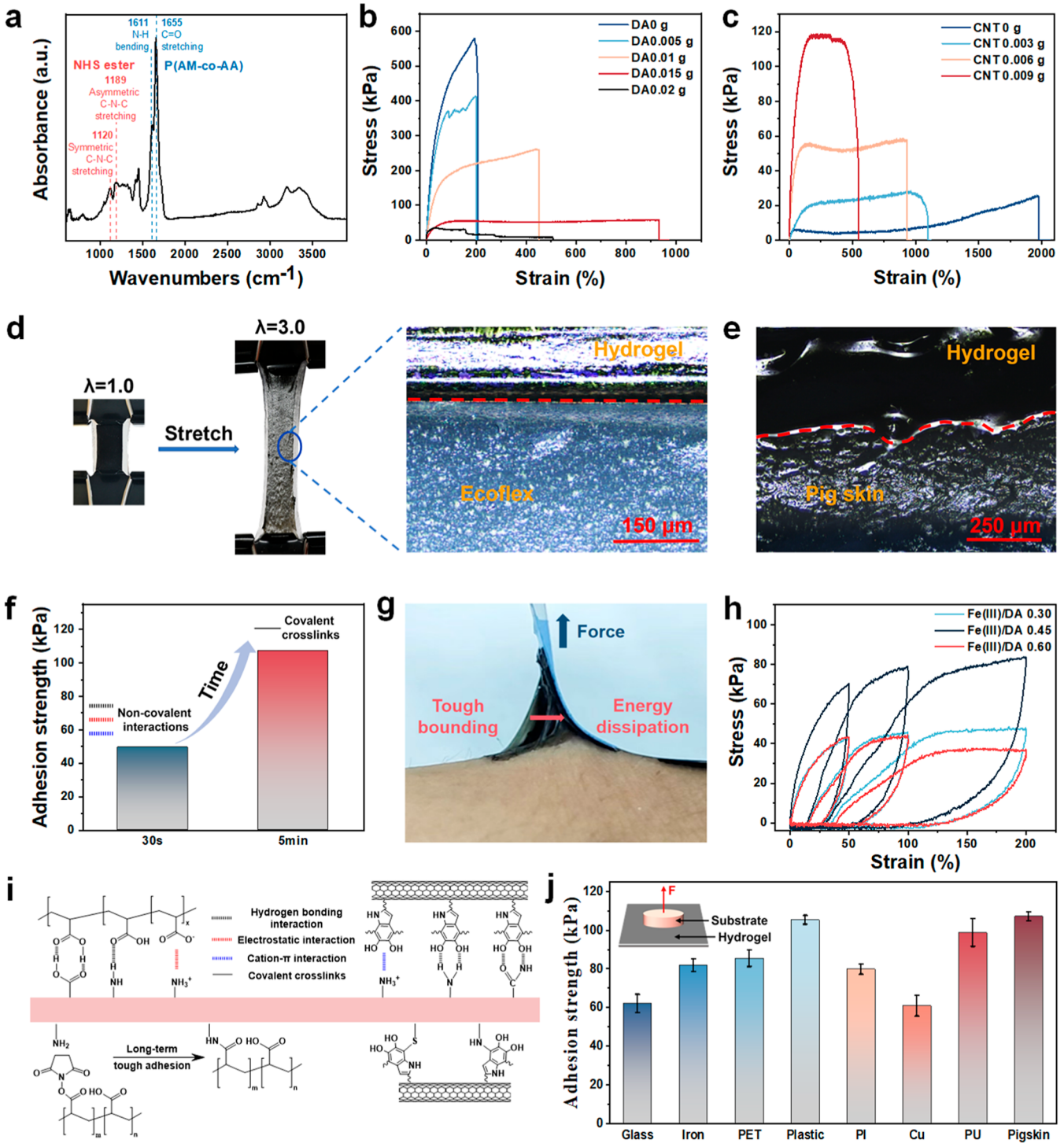

Figure 2. Mechanical properties and adhesion performances of PAACP conductive hydrogels. (a) FTIR spectra of PAACP conductive hydrogel. (b) Tensile stress−strain curves of PAACP conductive hydrogels with different DA content. (c) Tensile stress−strain curves of PAACP conductive hydrogels with different CNT-PDA content. (d) Photograph and confocal microscope image of PAACP conductive hydrogel when stretched 300% on Ecoflex elastomer. (e) Confocal microscope image of the cross-sectional interface between PAACP conductive hydrogel and pigskin. (f) Adhesive strength of PAACP conductive hydrogel in immediate adhesion (30 s) and long-term adhesion (>5 min). (g) Photographs of PAACP conductive hydrogel adhesion to skin. h) Cyclic tensile stress−strain curves of PAACP conductive hydrogels at varying Fe (III)/DA molar ratios. (i) Adhesion mechanism of PAACP conductive hydrogel. (j) Adhesive strength of PAACP conductive hydrogel with various materials.

filler content, while also exhibiting bioadhesive properties that ensure a conformable and stable bioelectronic interface, enabling long-term electrical communication with neural tissue and offering a promising approach for effective nerve repair.

To achieve this, the hydrogel should possess (1) high conductivity, allowing for efficient bidirectional electrical communication for both electrical recording and stimulation; (2) high bioadhesion, ensuring conformal contact with neural

https://doi.org/10.1021/acsnano.5c03336
ACS Nano 2025, 19, 18729−18746

tissue surfaces and maintaining interface stability; (3) nerve compatible elasticity, enabling mechanical matching with soft tissues; and (4) microfabrication compatibility, allowing easy integration with microfabricated bioelectronic devices.

Herein, we report a strategy for the design of conductive hydrogels by employing a copolymer network of acrylamide and acrylic acid as the foundational structure (Figure 1). The absence of rigid structures, such as benzene rings, along with the lack of long side chains imparts high flexibility to the polymer chains, thereby enabling the hydrogel to attain a low tensile modulus (~100 kPa), high stretchability (~1000%), and high toughness (7.33 kJ m^{-2}). Additionally, through the synergistic action of catechol and NHS ester functional groups, the hydrogel is endowed with strong immediate adhesion (49.53 kPa) and stable long-term adhesion (107.14 kPa), allowing it to form seamless contact with biological tissues. Furthermore, to enhance the uniform dispersion of carbon nanotubes within the gel matrix, polydopamine-modified carbon nanotubes (CNT-PDA) were introduced, which facilitated noncovalent interactions between the nanotubes and the polymer network. Notably, at a very low loading of 0.33 wt %, this approach resulted in a high conductivity of 9.52 S/m, promoting efficient ion-electron transfer at the gel−tissue interface. Compared to other conductive hydrogels (Figure 1d),[29−33] the PAACP conductive hydrogel demonstrates a comprehensive advantage in terms of conductivity, adhesive strength, tensile modulus, and elongation at break, which facilitates its application at the gel−tissue interface.

Leveraging these properties, we designed a gel-based cuff electrode (width: 500 μm) that adheres seamlessly to the murine sciatic nerve, enabling suture-free implantation and bidirectional electrical communication. To validate its therapeutic potential, we applied the PAACP conductive hydrogel to a murine sciatic nerve injury model. Unlike conventional electrical stimulation methods, which often depend on open-loop paradigms or acute postinjury interventions under anesthesia, our approach integrates the PAACP conductive hydrogel into a closed-loop neuromodulation system. This innovation allows real-time, feedback-driven electrical stimulation tailored to dynamic physiological states, including during the awake state, thereby optimizing therapeutic precision. By fine-tuning stimulation parameters through this adaptive system, we achieved accelerated repair of sciatic nerve injuries. Together, the PAACP conductive hydrogel addresses critical challenges in bioelectronics, offering a platform for stable, long-term interfacing and activity-dependent neuromodulation. This advancement simplifies surgical workflows while enabling precise, closed-loop therapies, paving the way for transformative applications in bioelectronic medicine.

RESULTS AND DISCUSSION

Design and Preparation of Highly Conductive and Self-Adhesive Stretchable Hydrogel. In the design of the conductive hydrogel, we focused on three fundamental aspects: the backbone structure, conductive fillers, and adhesive functional groups. We utilized a copolymer network of acrylamide and acrylic acid for the hydrogel backbone, primarily due to its unique combination of mechanical flexibility and biocompatibility. The mechanical flexibility of the PAM−PAA matrix is intricately governed by the ratio of acrylamide to acrylic acid in its composition. Acrylamide imparts mechanical strength to the matrix, while an increased proportion of acrylic acid enhances its flexibility. The hydrogen bonding interactions between the carboxyl groups (−COOH) of acrylic acid and the amide groups ($-CONH_2$) of acrylamide further reinforce the network's toughness. Moreover, the PAM−PAA matrix is widely recognized for its excellent biocompatibility.[34,35] It does not exhibit toxic effects on human fibroblasts and is characterized by being noncarcinogenic, nontoxic, and nonallergenic. These properties render it highly suitable for medical applications, including drug delivery systems, wound healing, and tissue engineering. Additionally, the backbone structure is inherently stable and readily modifiable, allowing for flexible adjustments and optimizations to enhance performance.

To improve the conductivity of the hydrogel, we opted for single-walled carbon nanotubes (SWCNTs) as conductive nanofillers. The crucial factor in improving the conductivity of this system lies in increasing the content of CNTs and ensuring their uniform dispersion within the hydrogel matrix. However, due to the strong hydrophobic interactions between individual carbon nanotubes, unmodified CNTs tend to aggregate within the hydrogel, resulting in poor dispersion (Figure S1a). Surface modification has been demonstrated to be effective in improving CNT dispersion and reducing cytotoxicity. Among various techniques, dopamine coating stands out as a simple and efficient method for modifying the surface of CNTs.[33,36] By introducing polydopamine (PDA)-modified CNTs, we significantly enhanced their dispersion in aqueous solutions (Figure S1b) and established an effective electronic conductive network at lower CNTs contents. This not only imparts high conductivity to the hydrogel but also enhances its mechanical properties by acting as a nanoreinforcement. Additionally, the catechol groups in dopamine provide a degree of adhesiveness. To further improve the adhesion of the hydrogel to wet tissue surfaces, we modified the hydrogel backbone by grafting it with *N*-hydroxysuccinimide (NHS) ester, facilitating stable adhesion to moist tissue surfaces. Fourier-transform infrared spectroscopy (FTIR) analysis confirmed the presence of the −N−H bending vibration at 1611 cm^{-1} and the −C═O stretching vibration at 1655 cm^{-1}, characteristic of the backbone structure. Additionally, the successful incorporation of NHS ester groups was indicated by the symmetric C−N−C stretching vibration at 1120 cm^{-1} and the asymmetric C−N−C stretching vibration at 1189 cm^{-1} (Figure 2a).[37] Through this multifaceted design strategy, we successfully developed a conductive hydrogel system with high conductivity, self-adhesiveness, and stretchability, laying a solid foundation for its application in the fields of electrophysiological monitoring and therapy.

The hydrogel was synthesized using a straightforward two-step process. In the initial step, polydopamine-modified carbon nanotubes (CNT-PDA) were prepared *via* Fe^{3+}-induced polymerization of dopamine (DA). Ferric chloride ($FeCl_3$), acting as a potent oxidizing agent, initiates the oxidation of DA and facilitates the transformation of 5,6-dihydroxyindole into the corresponding quinone through hydrogen abstraction.[38] Once DA has polymerized into polydopamine (PDA) in solution, noncovalent interactions between CNTs and PDA chains effectively modify the surface of the carbon nanotubes, resulting in the formation of CNT-PDA. It is important to note that some catechol groups remain unoxidized in the CNT-PDA structure, which are crucial for the hydrogel's adhesive properties. Consequently, the quantity of the oxidizing agent ($FeCl_3$) must be meticulously controlled to ensure the desired functionalization.

In the subsequent step, acrylamide monomer, acrylic acid monomer, and *N*-Succinimidyl Methacrylate (AAc-NHS) were

https://doi.org/10.1021/acsnano.5c03336
ACS Nano 2025, 19, 18729−18746

uniformly mixed in PBS buffer. This mixture was then added to the dispersion of CNT-PDA. The polymerization process was initiated by adding ammonium persulfate (APS) as the initiator, *N*,*N*′-methylenebis(acrylamide) (MBA) as the cross-linker, and *N*,*N*,*N*′,*N*′ -tetramethylethylenediamine (TEMED) as the initiator accelerator. The resulting mixture underwent radical polymerization and cross-linking at 40 °C in an oven for 120 min. This process yielded a P(AM-*co*-AA)-CNT-PDA hydrogel, named $PAA_xC_yP_z$ (where *x*, *y*, and *z* correspond to the mass ratio of acrylic acid to acrylamide, the mass of CNTs added, and the mass of DA incorporated, respectively), which exhibits a modulus comparable to that of biological tissues, along with excellent wet adhesion and high electrical conductivity. Additionally, PAACP-Fe_a and PAACP-AAc-NHS_b hydrogels (where a and b represent the molar ratios of $FeCl_3$ to DA and the mass of AAc-NHS added to the hydrogel, respectively) were prepared under identical conditions. The recipes for the different component hydrogels are provided in Table S1.

Mechanical Properties of PAACP Conductive Hydrogel. The backbone structure of the PAACP conductive hydrogel is formed through the copolymerization of acrylamide and acrylic acid, resulting in a network abundant in amino and carboxyl groups. The CNT-PDA interacts with the PAM−PAA polymer network *via* interactions between the catechol groups of PDA and the amino and carboxyl groups, thereby enhancing the mechanical properties of the hydrogel system.

A key factor influencing the tensile modulus of the hydrogel is the ratio of acrylic acid to acrylamide. We selected hydrogel systems with varying acrylic acid/acrylamide mass ratios of 0%, 10%, 20%, and 30% for tensile stress−strain testing (Table S2). The carboxyl groups in the poly(acrylic acid) component can form physical cross-linking points through hydrogen bonding and electrostatic interactions with the amide groups in the polyacrylamide component. These physical cross-linking increase the cross-linking density of the hydrogel, thereby improving the tensile modulus of the material. As shown in Figure S2a, the pure polyacrylamide hydrogel, without acrylic acid, exhibits poor mechanical properties, with a tensile modulus of only 23.33 kPa. As the proportion of acrylic acid increases, the interactions between poly(acrylic acid) and polyacrylamide introduce additional physical cross-linking in the hydrogel network, significantly increasing the cross-linking density. These extra physical cross-linking effectively absorb and dissipate energy, allowing the hydrogel to withstand larger deformations without fracturing, thereby improving its mechanical performance, as reflected by an increase in tensile modulus to 89.26 kPa. However, when the acrylic acid content reaches a certain threshold, the interaction between poly(acrylic acid) and polyacrylamide becomes saturated. Further increases in acrylic acid content do not significantly enhance the number of physical cross-linking points and may even decrease the overall cross-linking density, leading to a reduction in tensile modulus (75.79 kPa). Consequently, we fixed the acrylic acid/acrylamide mass ratio at 20% to further investigate the effect of other substances on the mechanical properties of the hydrogel.

Incorporating CNT-PDA into the hydrogel matrix not only enhances electrical conductivity but also serves as a nanofiller to improve the mechanical properties of the hydrogel. As shown in Figure 2b, tensile stress−strain tests were performed under different contents of DA. Specifically, as the DA content increases from 0 to 0.015 g, the tensile modulus of the hydrogel decreases significantly from 991.28 to 89.26 kPa, while the elongation at break increases from 195.09% to 932.39%. With the increase of DA content, the dispersion of CNT-PDA within the hydrogel matrix is improved, effectively alleviating the aggregation effect of CNTs. This leads to a reduction in the rigid support structures formed by CNTs, thereby lowering the modulus of the material.[33,39] However, upon further increasing the DA content to 0.02 g, the reducibility of DA molecules interferes with the activity of the initiator APS, thereby inhibiting the free radical polymerization of the monomer.[40,41] This results in an incomplete polymerization process and renders the $PAA_{0.2}C_{0.006}P_{0.02}$ conductive hydrogel inhomogeneous (Figure S2b,c). Based on these observations, we opted for a CNT/DA mass ratio of 2:5 to disperse CNTs effectively.

Subsequently, tensile stress−strain tests were performed on hydrogels with varying CNT-PDA contents, as illustrated in Figure 2c. The results indicate that as the CNT-PDA content increases, the tensile modulus of the PAACP conductive hydrogels gradually increases, while the elongation at break decreases. This trend can be attributed to the high rigidity of CNTs and their interactions with the polymer chains. The nano reinforcement effect of CNT-PDA contributes to the strengthening of the hydrogel network structure,[36] thereby enhancing its tensile modulus. Additionally, due to the noncovalent interactions between CNT-PDA and the PAM−PAA chains, the hydrogel is able to better dissipate energy during deformation, resulting in a high toughness of 7.33 kJ m^{-2}. This value is significantly higher than the toughness of human skin (~1.8 kJ m^{-2}) and typical PAM hydrogels (~10−250 J m^{-2}).[42,43] To achieve an optimal balance between the mechanical and electrical properties of the hydrogel, we selected the $PAA_{0.2}C_{0.006}P_{0.15}$ hydrogel for further experimentation.

Building on these mechanical properties, we next investigated the stability of the PAACP conductive hydrogel under high strain. As demonstrated in Figures 2d and S3, we applied the prepared PAACP conductive hydrogel attached to an Ecoflex elastomer for tensile testing. Even when stretched to approximately 300%, the hydrogel maintained tight adhesion to the elastomer, with no separation at the interface edge, as confirmed by confocal microscopy imaging. This ability to preserve structural integrity under high strain highlights its potential application in stretchable electronic devices.

Upon the application of the hydrogel, the interfacial water forms a barrier between the tissue and the hydrogel, significantly impeding rapid and robust adhesion. Compared to traditional adhesive hydrogels, wet-adhesive hydrogels possess the capability to maintain stable adhesion under wet conditions, enabling their application in physiological environments *in vivo* and expanding their potential usage scenarios. Hydrogels with robust wet-adhesive properties generally require the following characteristics: (1) abundant adhesive functional groups; (2) the capacity to induce a dehydration effect that eliminates water from the hydrogel−tissue interface; and (3) strong internal cohesion.[44]

As shown in Figure 2e, our PAACP conductive hydrogel demonstrates strong adhesion to pigskin at the interface. The poly(acrylic acid) component in the PAACP network can absorb interfacial water from wet tissue surfaces in less than 30 s under mild pressure of approximately 1 kPa, effectively drying the tissue surface. Concurrently, the poly(acrylic acid) network of the hydrogel provides an abundance of carboxyl groups, which can form immediate physical cross-linking with the tissue surface through mechanisms such as hydrogen bonding and electrostatic interactions. Upon contact with the substrate, the catechol groups in PDA form physical cross-links, including

https://doi.org/10.1021/acsnano.5c03336
ACS Nano 2025, 19, 18729−18746

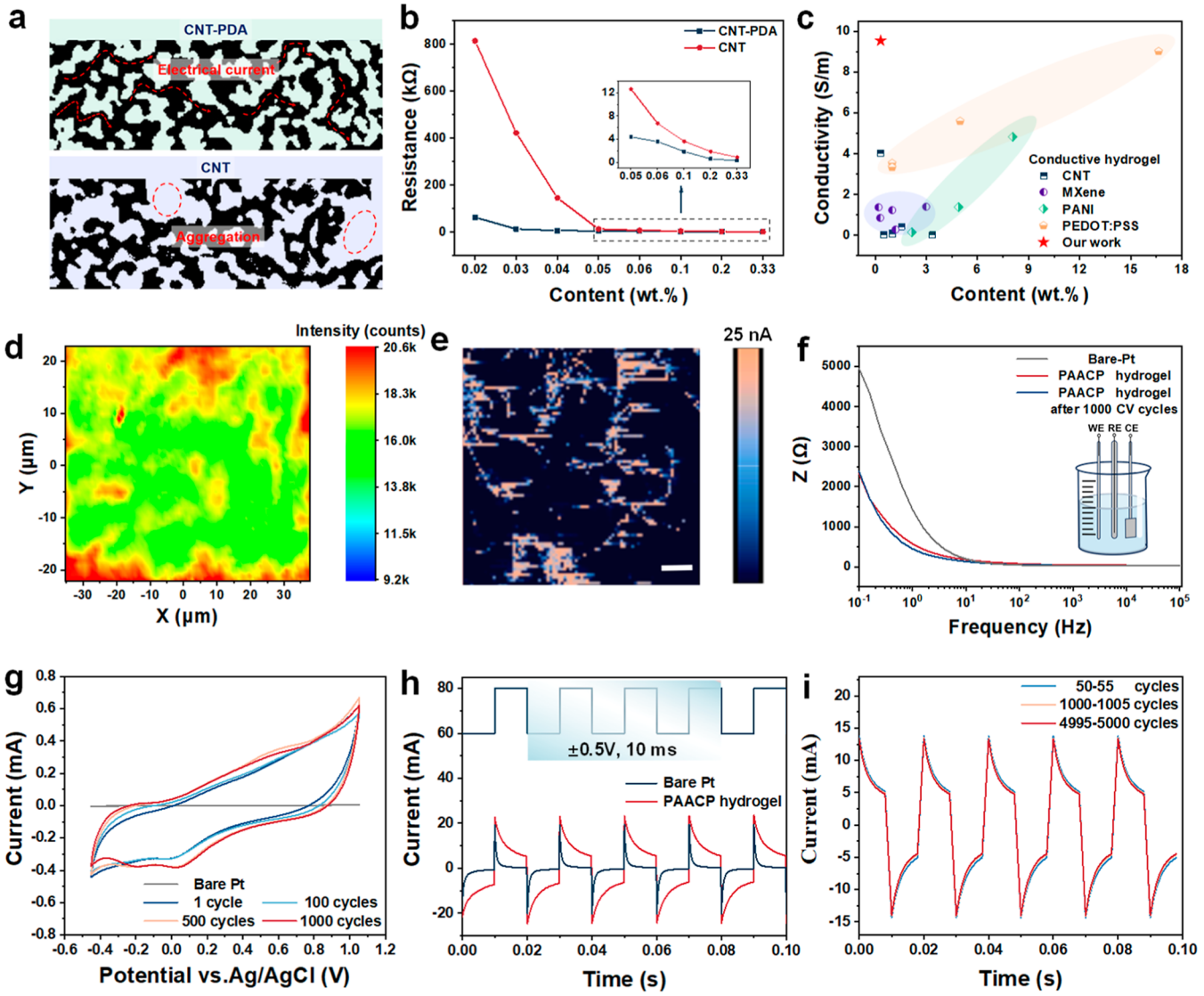

Figure 3. Electrical performances of PAACP conductive hydrogels. (a) PAACP conductive hydrogel and PAAC conductive hydrogel with conductive filler content of 0.02 wt %. (b) Resistance of PAACP conductive hydrogels and PAAC conductive hydrogels with different contents of conductive fillers, with specific resistance values listed in Table S4. (c) Comparison of conductive filler content and conductivity of different conductive hydrogels. (d) Raman Mapping of PAACP conductive hydrogel. (e) AFM current images of PAACP conductive hydrogel. Scale bar, 1 μm. (f) Electrical impedance spectra of PAACP conductive hydrogel and Pt wire electrode. (g) Long-term cyclic voltammetry curves of PAACP conductive hydrogel and Pt wire electrode at a scan rate of 100 mV s^{-1}. (h) CIC curves of PAACP conductive hydrogel and Pt wire electrode at a frequency of 50 Hz with biphasic pulses of ±0.5 V. (i) CIC curves of PAACP conductive hydrogel at 50, 1000, and 5000 cycles.

hydrogen bonds and cation−π interactions, which enable the hydrogel to adhere to other surfaces. As shown in Figure 2f, within 30 s of contact between the hydrogel and the wet pigskin surface, the adhesive strength reaches 49.53 kPa, primarily due to noncovalent interactions. Stable wet adhesion between hydrogels and biological tissues is generally achieved *via* covalent bonding. Nucleophilic groups such as amines and sulfhydryl groups are present on biological tissue surfaces. Oxidized catechol groups (dopaquinone) can slowly form covalent bonds with primary amines and thiol groups, thereby significantly enhancing tissue adhesion strength.[45] Additionally, covalently cross-linked poly(acrylic acid) *N*-hydroxysuccinimide ester (PAA-NHS) has been employed to synergistically enhance bioadhesion in conjunction with catechol functional groups. The NHS ester group exhibits high reactivity with primary amines due to its electron-withdrawing nature. The succinimide ring stabilizes the intermediate during the reaction, making NHS ester an efficient coupling agent for forming covalent bonds. As the adhesion time increases, the NHS ester groups grafted onto the acrylic acid in the hydrogel react with primary amine groups on the tissue surface through coupling reactions, forming covalent cross-links within minutes.[46] Over time, the formation of these covalent bonds further enhances the adhesive strength, reaching 107.14 kPa after 5 min. This time-dependent increase in adhesive strength offers significant advantages for practical surgical applications, as it allows for greater tolerance in repositioning the hydrogel during initial attachment. Moreover, this feature improves the stability of the hydrogel over long periods of use, ensuring reliable adhesion throughout the process.

In addition to the noncovalent and covalent bonding mechanisms described above, the cohesive strength of the hydrogel is further enhanced by the incorporation of coordination interactions and electrostatic forces, which

https://doi.org/10.1021/acsnano.5c03336
ACS Nano 2025, 19, 18729−18746

contribute to the overall stability and performance of the adhesive system. The catechol groups can form dynamic coordination bonds with metal ions (*e.g.*, Fe^{3+}, Cu^{2+}), creating cross-linked networks. This coordination not only enhances the cohesive forces within the material, but also through the reversible dissociation of these bonds, dissipates energy and improves the material's toughness.[47] During the formation of CNT-PDA induced by Fe(III)-oxidation, coordination bonds are established between Fe(III) and the catechol functional groups of polydopamine. Moreover, electrostatic interactions occur between Fe(III) and the carboxylate groups (COO^-) within the PAM−PAA backbone network. The introduction of $FeCl_3$ enhances the cohesive strength of the system, as evidenced by the energy dissipation illustrated in Figure 2g. This increased energy dissipation subsequently improves the adhesive strength of the hydrogel system. We evaluated stretch-release cycling curves for PAACP conductive hydrogels at various molar ratios of ferric chloride ($FeCl_3$) to dopamine. At a molar ratio of 0.15, the oxidation of dopamine is incomplete due to insufficient Fe(III), leading to a significant presence of unpolymerized dopamine within the system. This excess of unpolymerized dopamine negatively impacts the activity of the initiator APS, thereby compromising the gelation process (Figure S4a).[40,41] As shown in Figure 2h, when molar ratios of $FeCl_3$/dopamine are set at 0.3, 0.45, and 0.6, notable energy dissipation is observed within the system during load-unload cycles. Initially, as the Fe(III) content increases, the energy dissipation also increases. However, this trend reverses when the Fe(III) content becomes excessive, which is attributed to a transition from DOPA-Fe(III) tris-complexes to DOPA-Fe(III) monocomplexes. In Figure S4b, we measured adhesive strength across different molar ratios of $FeCl_3$ to dopamine. The unoxidized catechol groups in CNT-PDA play a critical role in the adhesion properties of the hydrogel. However, an increase in Fe(III) content correlates with a decrease in unoxidized catechol groups and consequently reduces adhesive strength. Therefore, we selected the PAACP conductive hydrogel with a Fe(III)-to-DA molar ratio of 0.3 for subsequent experiments.

Given that DA and AAc-NHS are the key functional groups enabling stable adhesion through the formation of covalent bonds with the substrate, we investigated the adhesive strength of PAACP conductive hydrogels under varying contents of DA and AAc-NHS (Figure S4c,d). Within the permissible gelation range, the adhesive strength of the hydrogel increases progressively with higher DA content. On the other hand, as the content of AAc-NHS increases, the adhesive strength initially rises, reaching its highest value at a content of 0.015 g, but subsequently declines, likely due to the saturation of AAc-NHS grafting onto acrylic acid. The detailed adhesion mechanism is demonstrated in Figure 2i.

The PAACP conductive hydrogel exhibits excellent adhesive strength and good substrate adaptability. As an interfacial adhesive, it is capable of naturally supporting a weight of 500 g and demonstrates strong adhesion to various non biological materials as well as biological tissues, as shown in Figure S4e. Even after being immersed in a wet environment for 24 h, it retains stable adhesion (Movie S1). The adhesive strength of the conductive hydrogel was tested on various substrates, as illustrated in Figure 2j, including glass, stainless steel, PET, plastic, PI, Cu, PU, and pigskin, all of which exhibits a high adhesive strength of over 60 kPa. During the tensile adhesive strength tests of biological tissues such as the heart and liver, due to their low modulus, specific measurable adhesive strength values were not obtainable. Actually, during the tensile process, interface failure occurred within the soft biological tissue, while the hydrogel−tissue interface maintained strong adhesion, indicating its good bioadhesive capability (Figure S4f).

Electrical Properties of the PAACP Conductive Hydrogel. To facilitate bidirectional communication between neural tissues and bioelectronic devices, PAACP conductive hydrogels must demonstrate stable electrical properties. The inherent high conductivity of CNT, combined with PDA modification, ensures the uniform dispersion of CNT-PDA throughout the hydrogel matrix. This results in the formation of continuous conductive pathways, establishing an efficient electron conducting network. We fabricated PAACP conductive hydrogels with varying CNT-PDA content, as well as PAAC conductive hydrogels with different CNT content. As shown in Figure S5, the surface of hydrogels without PDA modification appear rough, whereas those modified with PDA display a smooth and uniform surface. Subsequently, we focused on evaluating the performance of hydrogels at low conductive filler contents (0.01 wt %−0.06 wt %). Taking the conductive filler content of 0.02 wt % as an example (Figure 3a), it can be observed that the uniform dispersion of CNT-PDA within the hydrogel matrix leads to the formation of a more homogeneous and continuous electron conducting network. In contrast, due to aggregation, CNT fails to form a continuous electron conducting network in PAAC hydrogels at the same filler content. Detailed images of hydrogels with low conductive filler contents (0.01 wt %−0.06 wt %) are shown in Figures S6 and S7.

In addition, we measured the resistance of PAACP conductive hydrogels and PAAC conductive hydrogels with varying filler contents. As shown in Figure 3b, the resistance of PAACP conductive hydrogels is consistently lower than that of PAAC conductive hydrogels at all tested contents. Specifically, when the CNT-PDA content reaches 0.03 wt %, a significant drop in resistance is observed, indicating the achievement of the percolation threshold and the formation of an effective conductive network that reduced resistance. In contrast, for PAAC conductive hydrogels, the percolation threshold is not reached until the CNT content increases to 0.05 wt %. These resistance measurement results are consistent with the phenomena observed in the images of hydrogels with low conductive filler contents (0.01 wt %−0.06 wt %).

As the CNT-PDA content increases further, the resistance continues to decrease, highlighting the significant influence of CNT-PDA content on the electrical properties of the hydrogel. Compared to existing conductive hydrogels doped with nanoconductive fillers, our PAACP conductive hydrogel achieves a relatively high conductivity of 9.52 S/m at a low filler content of 0.33 wt % (Figure 3c).[29−31,39,48−61] Although hydrogels doped with PEDOT:PSS exhibit higher electrical conductivity, they typically require much higher doping levels, with some even comprising pure PEDOT:PSS hydrogels.[62] The lower filler content in our hydrogels enhances biocompatibility. To evaluate the local tissue response following implantation, sciatic nerves were harvested from mice 7 days postsurgery and analyzed by immunofluorescence staining for neurofilaments (NF200), Schwann cells (S-100), and macrophages (Iba-1). Experimental groups included implantation of the PAACP cuff electrode, a sham surgery (no implant), and implantation of a size-matched commercial cuff electrode (800 μm inner diameter) as a positive control. Quantitative analysis revealed no significant differences in Schwann cell density (S-100+) or axonal integrity (NF200+) between the PAACP cuff and sham

https://doi.org/10.1021/acsnano.5c03336
ACS Nano 2025, 19, 18729−18746

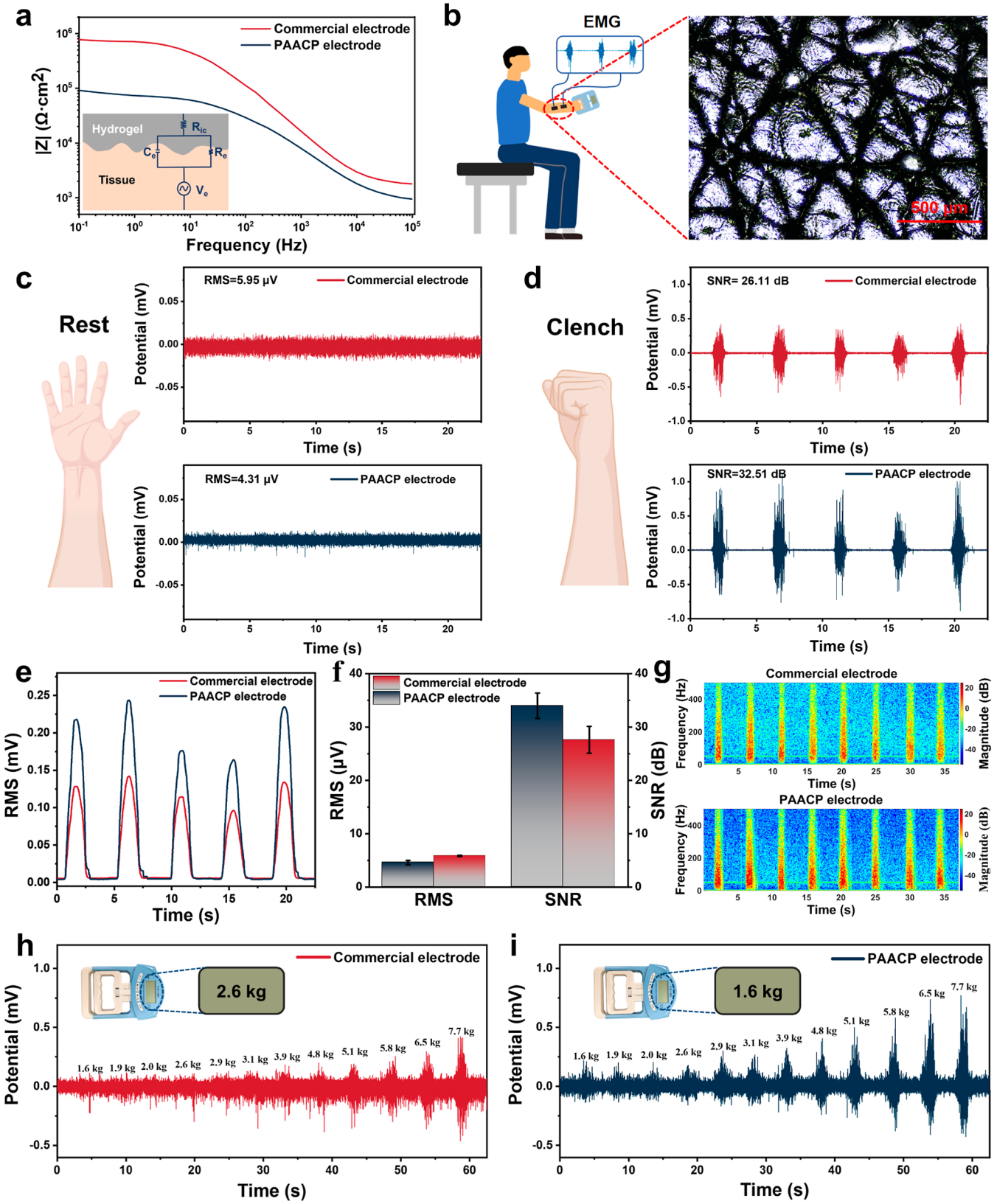

Figure 4. Recording of sEMG signals *in vitro*. (a) Skin-electrode interface impedance of PAACP electrode and commercial electrode (a representative result from one of three independent tests, detailed test results are shown in Figure S10), with the inset showing the hydrogel–tissue interface equivalent circuit model, where Ric represents the interconnect resistance of the higher order electronic circuitry connected to the electrode, and Ve represents the electric potential within the electrolytic medium.64 (b) Schematic illustration of sEMG signal testing, with the inset showing a confocal microscope image of the skin texture replicated by the PAACP electrode after testing. (c,d) Time-domain plots of sEMG measured under resting and repetitive fist clenching conditions. (e) RMS values under repetitive fist clenching states. (f) Baseline noise

https://doi.org/10.1021/acsnano.5c03336
ACS Nano 2025, 19, 18729–18746

Figure 4. continued

and signal-to-noise ratio of PAACP electrode and commercial electrode. (g) Time-frequency plots of sEMG measured under repetitive fist clenching conditions. (h,i) sEMG signals under gradually increasing grip strength using a dynamometer.

groups (Figure S8a−c). In contrast, the positive control group displayed significant Schwann cell loss and axonal damage. Furthermore, Iba-1 expression, indicative of macrophage infiltration, was comparable between the PAACP cuff and sham groups, whereas a marked increase in Iba-1+ cells was observed in the positive control group (Figure S8a,d). These results demonstrate that the PAACP cuff electrode induces significantly less tissue damage and inflammatory response compared to the commercial cuff electrode, highlighting the favorable biocompatibility of the PAACP hydrogel for neural interface applications.

We utilized Raman mapping and Conductive Atomic Force Microscopy (C-AFM) to confirm the uniform dispersion of CNT-PDA as a conductive filler within the hydrogel matrix. The Raman spectrum of the PAACP conductive hydrogel exhibits a prominent peak at 1590 cm^{-1}, corresponding to the G-band of carbon nanotubes (Figure S9a). Based on this, we selected the 1590 cm^{-1} peak for Raman mapping analysis. As shown in Figure 3d, the selected region displays consistent Raman activity corresponding to carbon nanotubes, confirming the uniform distribution of CNT-PDA within the conductive hydrogel. Moreover, AFM current images (Figure 3e) further supported these findings, demonstrating that CNT-PDA establishes effective pathways for electron transfer.[5] In addition, we measured the $\Delta R/R_0$ of PAACP conductive hydrogels under a strain of 30% with varying DA contents (Figure S9b). The more uniformly dispersed CNT-PDA exhibits a smaller $\Delta R/R_0$ under the same strain, indicating improved stability in electrical properties.

The electrochemical performance of bioelectrodes plays a crucial role in the efficiency of electrophysiological signal transmission at the electrode-tissue interface.[63] To systematically evaluate the electrochemical properties of the PAACP conductive hydrogel, we integrated it onto a platinum wire electrode and immersed it in PBS buffer solution. Its electrochemical stability was investigated using cyclic voltammetry (CV), electrochemical impedance spectroscopy (EIS), and charge injection capacity measurements (CIC). The detailed testing methods are described in the Methods section. As shown in Figure 3f, the electrochemical impedance spectrum reveals that the PAACP conductive hydrogel exhibits significantly lower impedance than the platinum wire electrode in the low-frequency range (<100 Hz). In the high-frequency range (10^3 to 10^6 Hz), the impedance values of the PAACP conductive hydrogel and the platinum wire electrode are comparable. This is attributed to the ability of the PAACP conductive hydrogel to transmit charge *via* both electronic and ionic mechanisms, resulting in a substantial reduction in impedance. Notably, even after 1000 cyclic voltammetry (CV) cycles, the electrochemical impedance spectrum demonstrates that the PAACP conductive hydrogel maintains a low impedance, further highlighting its stability and durability. Charge storage capacity (CSC) is commonly used to predict the amount of charge an electrode can inject during stimulation to activate neural tissue. At a scan rate of 100 mV/s, the PAACP conductive hydrogel exhibits a CSC of 6.08 mC/cm^2, while, by comparison, a platinum electrode scanned at the same rate displays a CSC of only 6.60 $\mu C/cm^2$ (Figure 3g). A higher CSC indicates a greater charge transfer capability and increased signal intensity. Over 1000 cycles, the CV curve of the PAACP conductive hydrogel shows minimal variation, indicating its electrochemical stability. To further evaluate its neuromodulation capacity, the charge injection capacity (CIC) of PAACP conductive hydrogel was characterized. Under short biphasic pulse electrical stimulation (10 ms), the PAACP conductive hydrogel exhibits a CIC value of 437.85 $\mu C/cm^2$, significantly higher than that of the platinum wire electrode, which shows a CIC of 64.53 $\mu C/cm^2$ (Figure 3h). This indicates that the PAACP conductive hydrogel can facilitate charge transfer, effectively stimulating nerve tissue. After 5000 cycles of biphasic charge injection (Figure 3i), the CIC value shows no significant decline, and no noticeable interface failure occurs, demonstrating the hydrogel's ability to maintain excellent electrical performance. In Table S3, we have compared the CSC and CIC values of the PAACP conductive hydrogel with those of other electrodes used for electrophysiological monitoring. This combination of high charge storage capacity and charge injection capacity, along with its inherent softness and wet adhesion, makes it particularly appealing for electrophysiological monitoring and stimulation.

***In Vitro* Recording of sEMG Signals.** Low skin-electrode contact impedance is essential for achieving high SNR and monitoring weak signals.[64] To evaluate this, PAACP conductive hydrogels were cut into 1 cm × 1 cm electrodes, with conductive copper−nickel tape used to connect the hydrogel to external circuitry. Before surface electromyography (sEMG) signal collection, we tested the skin-electrode contact impedance across the frequency range of 0.1 to 10^5 Hz (Figure 4a). The inset in Figure 4a shows a simplified electrode-tissue interface model, where the contact impedance can be represented by a parallel circuit consisting of a leakage resistance (Re) and a capacitance (Ce). Since muscle electrical signals primarily lie within the frequency range of 10−500 Hz, we focused on the impedance values at low frequencies. The skin-electrode contact impedance of the commercial electrodes is 428.88 ± 36.29 $k\Omega \cdot cm^2$ at 10 Hz, while that of the PAACP electrodes is 60.80 ± 2.92 $k\Omega \cdot cm^2$ at 10 Hz, which is only about one-seventh of that of the commercial electrodes (Figure S10). This reduction in contact impedance is attributed to the PAACP electrode's low modulus, high adhesion, and superior conductivity, indicating better conformity with the skin, which is highly advantageous for recording weak electromyographic signals from subtle muscle movements. Figures 4b and S11a illustrate the schematic of the sEMG signal testing and the placement of the electrodes. As shown in the inset, the PAACP electrode accurately replicates the texture of the skin, while the commercial gel electrode is unable to replicate clear skin texture (Figure S11b). This further confirms the seamless contact between the PAACP electrode and the skin. Additionally, Figure S11c demonstrates that the PAACP conductive hydrogel can be removed cleanly from the skin surface without leaving any residue, reinforcing its suitability for human skin applications.

We subsequently compared the sEMG signals recorded by commercial electrodes and PAACP electrodes under resting and repetitive fist clenching conditions. The time-domain plots (Figure 4c,d) reveal that the PAACP electrode outperforms the commercial electrode in terms of lower baseline noise and

https://doi.org/10.1021/acsnano.5c03336
ACS Nano 2025, 19, 18729−18746

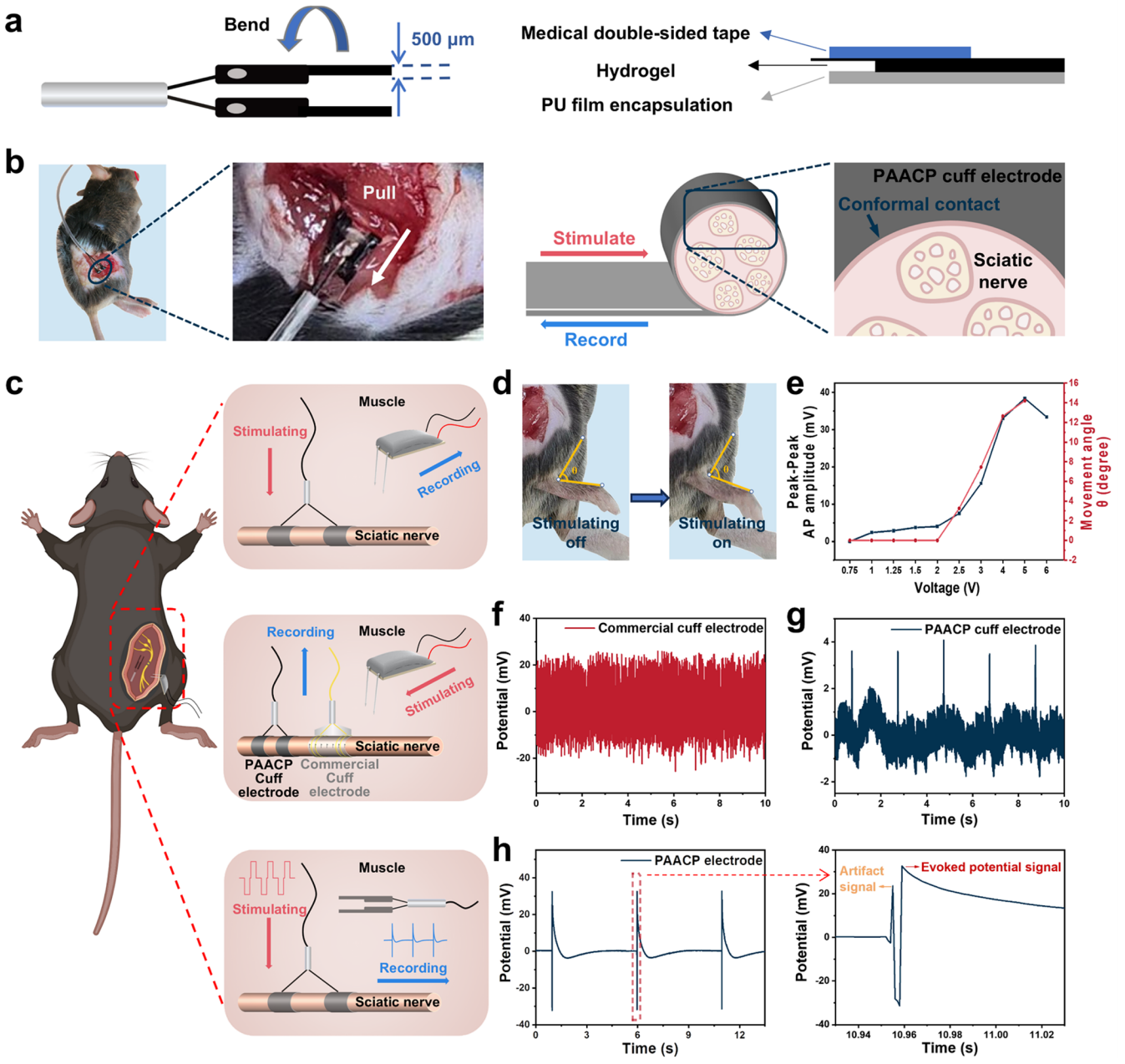

Figure 5. Stimulating and recording *in vivo*. (a) Schematic illustration showing the geometry and dimensions of the PAACP cuff electrode. (b) Photograph of PAACP cuff electrode implantation into sciatic nerve of mice and schematic illustration of hydrogel−nerve interface. (c) Schematic illustration of the *in vivo* stimulation and recording experiment (photographs of the actual setup are shown in Figure S13). Created with BioRender.com. (d) Photographs of ankle movement induced by stimulation through the PAACP cuff electrode. (e) Relationship between the peak-to-peak AP amplitude of electromyographic responses, ankle movement angle, and stimulation intensity. (f,g) CNAPs recorded by the PAACP cuff electrode and commercial cuff electrode (with a commercial bipolar needle electrode used as the stimulation electrode). (h) CMAPs recorded by the PAACP electrode.

higher signal amplitude. By extracting and comparing the root-mean-square (RMS) values under resting and repetitive fist clenching states (Figure 4e), we observe that the PAACP electrode achieves a low baseline noise of 4.31 μV and a high signal-to-noise ratio (SNR) of 32.51 dB, surpassing the 5.95 μV baseline noise and 26.11 dB SNR of the commercial electrode (Figure 4f). Furthermore, the time-frequency analysis reveals that the PAACP electrode displays more stable power distribution across different frequencies under the same motion conditions (Figure 4g).

Additionally, we tested the sEMG signals under gradually increasing grip strength using a dynamometer (Figure 4h,i and found that the PAACP electrode can detect muscle signals at grip strengths as low as 1.6 kg. Below this threshold, the signal can not be distinguished from background noise, whereas the commercial electrode's detection limit was 2.6 kg. These results further demonstrate the superiority of the PAACP electrode in recording sEMG signals from subtle muscle movements.

***In Vivo* Stimulation and Recording Using PAACP Cuff Electrodes.** To validate the bioelectronic functionality of the PAACP conductive hydrogel *in vivo*, we used laser cutting to

https://doi.org/10.1021/acsnano.5c03336
ACS Nano 2025, 19, 18729−18746

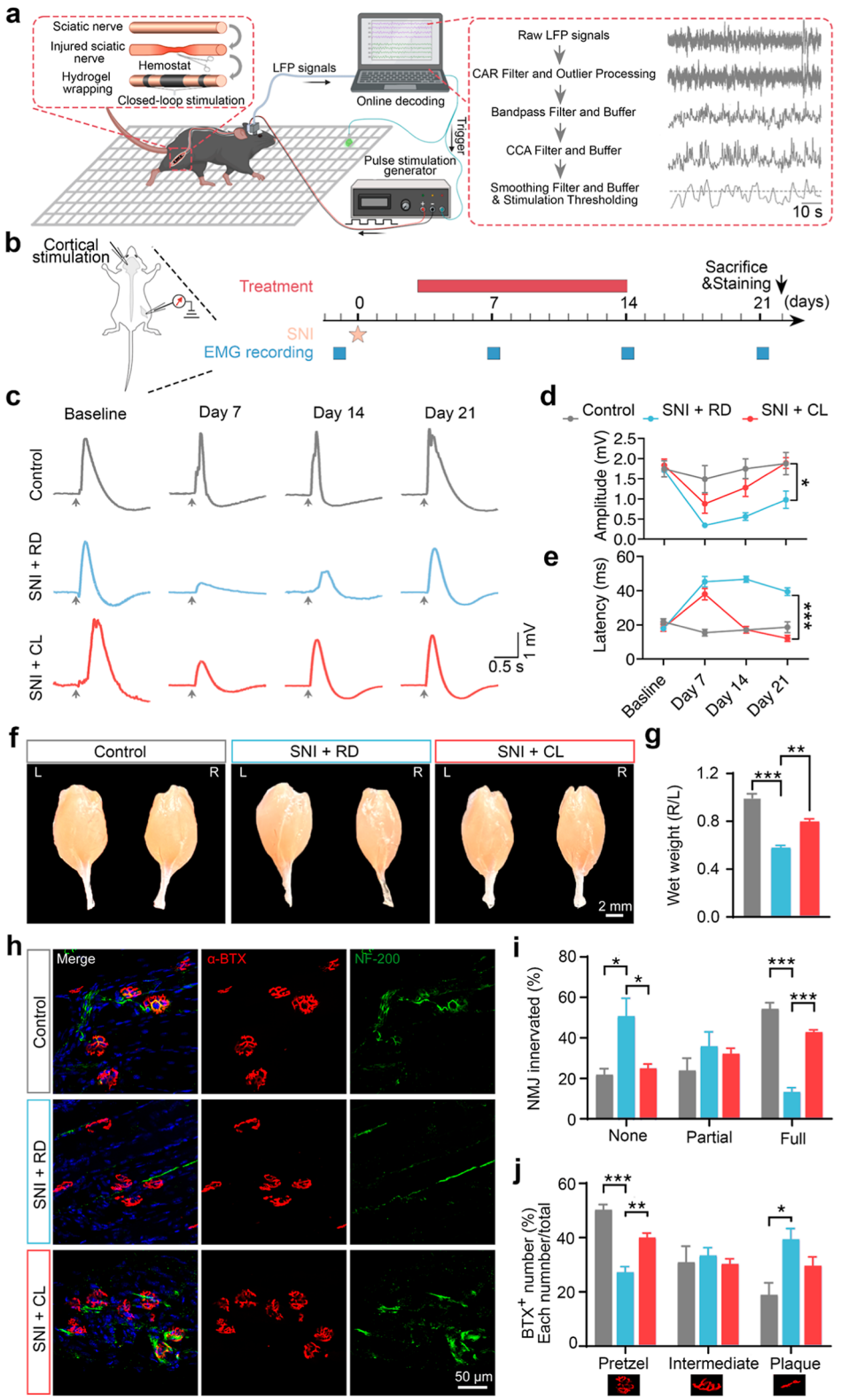

Figure 6. Closed-loop stimulation system demonstrates therapeutic efficacy in sciatic nerve injury repair. (a) Schematic illustration of the closed-loop neuromodulation setup in the awake state, utilizing the MEA electrode for real-time LFP recording, while the PAACP cuff electrode wraps around the injured sciatic nerve for stimulation. The system incorporates online signal processing and analysis algorithms for adaptive stimulation control. Created with BioRender.com. (b) Experimental timeline showing the 21 day treatment protocol with EMG recordings and final histological analysis. Created with BioRender.com. (c) Representative EMG waveforms from control, SNI + RD (random stimulation), and SNI + CL (closed-loop stimulation) groups at different time points, showing the evolution of muscle responses. (d,e) Quantitative analysis of EMG parameters including amplitude and latency across treatment groups over time. (f) Representative images of bilateral gastrocnemius muscles between uninjured (L) and injured (R) sides across three groups. Scale bar: 2 mm. (g) Quantitative analysis of gastrocnemius muscle wet weight ratio (R/L). (h) Immunofluorescence imaging of gastrocnemius muscle showing α-BTX (red) for NMJs and NF-200 (green) for

https://doi.org/10.1021/acsnano.5c03336
ACS Nano 2025, 19, 18729−18746

Figure 6. continued

regenerated nerve fibers. (i) Quantification of NMJs innervation patterns categorized as none, partial, or full reinnervation. (j) Morphological analysis of NMJs types classified as pretzel, intermediate, or plaque configurations, indicating more mature NMJs reformation in the closed-loop stimulation group. Scale bar: 50 μm. * for $p \leq 0.05$, ** for $p \leq 0.01$, * for $p \leq 0.001$. Image created with BioRender.com, with permission.**

shape it into a cuff electrode. The front end (electrode-tissue interface) was 500 μm wide, while the back end (electrode-wire connection) was 1 mm wide. The geometric structure of the PAACP cuff electrode is shown in Figure 5a. The upper and lower layers were respectively packaged with medical double-sided tape and medical PU film.

For the subsequent experiments, we used adult C57BL/6J mice weighing 20−25 g. The sciatic nerve surgeries on live mice were performed in accordance with the guidelines of the Songjiang Institute of the Shanghai Jiao Tong University School of Medicine. As illustrated in Figure 5b and Movie S2, during the implantation process, the PAACP cuff electrode did not require surgical suturing. Instead, it achieved conformal and robust adhesion to the sciatic nerve through simple folding, relying on its excellent bioadhesive properties. Even under tensile stress, the hydrogel−tissue interface remained stable, providing a foundation for achieving reliable bidirectional electrical communication.

First, we used the PAACP cuff electrode to stimulate the sciatic nerve and recorded the evoked compound muscle action potentials (CMAPs) of the leg muscles using a commercial bipolar needle electrode placed on the adjacent muscle. As shown in Figure 5c,d, periodic and stable ankle joint movements were observed under sciatic nerve electrical stimulation. The commercial bipolar needle electrode also accurately recorded electromyographic signals, producing consistent evoked CMAPs.

We further investigated the relationship between stimulation voltage and the peak-to-peak AP amplitude evoked by the PAACP cuff electrode. As illustrated in Figure S12a, the evoked CMAPs increase with increasing stimulation amplitude. Moreover, there is a high degree of consistency between the peak-to-peak AP amplitude and the ankle joint movement angle (Figure 5e), indicating good contact between the PAACP cuff electrode and the nerve. These results demonstrate the excellent stimulation performance of the PAACP cuff electrode.

To validate the ability of our PAACP cuff electrode to record neural signals, we applied a biphasic balanced pulse voltage (frequency: 0.5 Hz, pulse width: 1 ms, amplitude: 2 V) as stimulation using a commercial bipolar needle electrode. This was done to compare the performance of the PAACP cuff electrode and the commercial cuff electrode in recording compound nerve action potentials (CNAPs) from the sciatic nerve. The commercial cuff electrodes typically had a fixed inner diameter, requiring surgical sutures for implantation. Contact with the sciatic nerve was achieved through tightened pressure during the procedure, however, excessive baseline noise prevented the recording of CNAPs (Figure 5f). In contrast, the PAACP cuff electrode, owing to its superior conformal contact, was able to detect weak signals caused by respiration even in the absence of electrical stimulation (Figure S12b). Under biphasic balanced pulse voltage stimulation, the PAACP cuff electrode successfully recorded regular CNAPs from the sciatic nerve, indicating its excellent signal acquisition capabilities (Figure 5g). To further verify the recording performance of the PAACP cuff electrode, we recorded neural signals generated by shaking the legs of mice. Compared to the commercial cuff electrode, which failed to record neural signals, the PAACP cuff electrode consistently recorded regular sciatic nerve signals even after 7 days of implantation in mice (Figure S12c−e).

Finally, we used the PAACP cuff electrode to stimulate the sciatic nerve and recorded the evoked CMAPs of the leg muscles using a PAACP electrode placed on the adjacent muscle (Figure 5h). Similar to the results shown in Figure S12a, the PAACP electrode reliably recorded accurate and regular evoked CMAPs under sciatic nerve stimulation. The inset displays an enlarged waveform, where all the recorded signals show stimulus artifact signals, followed by the evoked CMAPs. Both the amplitude and the waveform of the CMAPs are almost the same for each electrical stimulation.[65] These results demonstrate that the PAACP neural electrode enables stable biphasic electrical communication and exhibits long-term reliability for neural modulation applications.

Closed-Loop Regulation Promoting Functional Recovery in Sciatic Nerve Injury. The repair of peripheral nerve injuries, particularly sciatic nerve injury (SNI), remains a formidable clinical challenge due to the limited regenerative capacity of peripheral nerves and the typically suboptimal functional recovery outcomes.[66] While electrical stimulation has emerged as a promising strategy to enhance nerve regeneration, conventional electrical stimulation techniques often rely on immediate postinjury applications or open-loop stimulation under anesthesia, which restricts their therapeutic efficacy and practical applicability.[67−69] Here, we addressed these limitations by developing a closed-loop neuromodulation system based on the PAACP cuff electrode, capable of dynamically regulating nerve regeneration through real-time neural activity feedback.

The conceptual framework and implementation of this closed-loop regulation system are depicted in Figure 6a. The injury site was wrapped with a PAACP conductive hydrogel, ensuring complete coverage and conformal contact with the sciatic nerve to facilitate both repair and electrical stimulation. Simultaneously, a microelectrode array (MEA) electrode was implanted in the M1 region of the mice brain to record local field potential (LFP) signals in real-time, which were processed in MATLAB. Following the method outlined in the work of Moritz,[70] the raw LFP signals were subjected to common Average Reference (CAR) filtering, bandpass filtering, canonical correlation analysis (CCA) filtering, and smoothing filtering to decode movement intention. Upon detecting movement intentions through threshold-based analysis, the system delivered precisely timed balanced biphasic pulses through the PAACP conductive hydrogel interface, creating a temporally synchronized therapeutic intervention. This synchronized electrical stimulation activated neurons across multiple levels of the motor descending pathway, from the cortex to the spinal cord, during movement, thereby enhancing functional connectivity and promoting repair of the injured sciatic nerve.

The feasibility of the closed-loop stimulation system was validated by conducting behavioral experiments on treated mice placed on a grid platform. During these experiments, LFP signals were recorded and decoded in real-time. When the decoded movement intentions exceeded the predefined threshold, one-

https://doi.org/10.1021/acsnano.5c03336
ACS Nano 2025, 19, 18729−18746

second electrical stimulation was delivered to the sciatic nerve *via* the PAACP cuff electrode. To visually indicate the stimulation process, a small indicator light was included in the system, which lit up simultaneously with each stimulation event. As shown in Movie S3, the decoded movement intention closely matched the actual movement behavior, confirming that our closed-loop stimulation system can be effectively used for subsequent experiments on SNI repair.

To evaluate the therapeutic efficacy of the closed-loop neuromodulation system, a 21 day treatment protocol was employed, comparing closed-loop (CL) and random (RD) stimulation paradigms in SNI mice models (Figure 6b). Mice received either CL or RD treatment from days 3 to 14 postinjury. Electrophysiological assessment through cortically evoked EMG revealed superior recovery dynamics in the SNI + CL group compared to the SNI + RD group. Specifically, the SNI + CL group exhibited markedly higher EMG amplitudes and reduced latencies (Figure 6c–e). By day 21 postoperation, the EMG amplitudes elicited by cortical stimulation in the SNI + CL group were comparable to those of the control group and significantly exceeded those of the SNI + RD group. Notably, the latencies in the SNI + CL group were slightly shorter than those of the control group and significantly shorter than those of the SNI + RD group. These findings suggest that closed-loop stimulation not only enhances nerve regeneration akin to traditional electrical stimulation but also facilitates neuronal reorganization and accelerates conduction velocity along the injured pathway. This enhanced cortical control over the injured limb highlights the ability of closed-loop stimulation to activate motor descending pathways, thereby improving motor control and functional recovery.

Subsequently, we analyzed the impact of different treatment strategies on muscles. Quantitative assessment of muscle atrophy through gastrocnemius muscle weight ratios (injured/uninjured) demonstrated significantly better muscle preservation in the SNI + CL group (79.6 ± 4.2%) compared to SNI + RD (57.9 ± 3.4%) at day 21 postinjury (Figure 6f,g). Immunofluorescence analyzes of neuromuscular junctions (NMJs), with α-BTX specifically labeling NMJs and NF-200 labeling regenerated nerve fibers, revealed substantial improvements in both NMJs innervation patterns and morphological maturation under the closed-loop stimulation. The SNI + CL group exhibited a significantly higher proportion of fully innervated NMJs (42.8 ± 1.2%) compared to the SNI + RD group (13.3 ± 2.1%), alongside a notable reduction in noninnervated NMJs (25.0 ± 2.0% in SNI + CL vs 50.8 ± 8.7% in SNI + RD) (Figure 6h,i). Moreover, morphological analysis demonstrated a predominance of mature pretzel-type NMJs in CL-treated animals (40.0 ± 1.6%), closely resembling the distribution pattern observed in the sham control group (50.3 ± 2.0%), and significantly exceeding that of the SNI + RD group (27.2 ± 2.0%) (Figure 6j). These histological findings collectively underscore the capacity of closed-loop stimulation to drive both structural and functional restoration of neuromuscular connectivity.

In summary, the closed-loop neuromodulation system, enabled by the PAACP cuff electrode, demonstrated profound efficacy in promoting functional recovery following SNI. By integrating real-time neural activity into the stimulation paradigm, this approach optimizes the temporal coupling between neural activity and therapeutic intervention, thereby enhancing both neural connectivity within the motor descending pathways and peripheral nerve regeneration. Furthermore, the closed-loop strategy mitigated injury-induced muscle atrophy and supported the re-establishment of mature neuromuscular connections. These results highlight the potential of activity-dependent stimulation paradigms to facilitate physiologically relevant and clinically translatable nerve repair strategies.

Despite the promising results of the PAACP conductive hydrogel-based closed-loop neuromodulation system in preclinical models, several clinical challenges remain to be addressed before its widespread adoption. These challenges include implantation stability, immune response, and long-term usage safety, which are critical for ensuring the effectiveness and safety of the system in human applications.

First, although the PAACP cuff electrode exhibits stable adhesion without suturing and minimal inflammatory responses in mice, long-term implantation stability in larger animal models or humans remains to be validated. Tissue encapsulation, mechanical stress from dynamic movements, and chronic immune reactions could compromise electrode performance over extended periods. To mitigate this, developing ultrathin biocompatible encapsulation layers may protect the electrode from tissue fluid infiltration while maintaining flexibility.

Second, the current PAACP conductive hydrogel lacks biodegradability, which may limit its utility in transient therapeutic applications. Future iterations could incorporate biodegradable polymers (*e.g.*, poly(lactic acid) (PLA) or poly(lactic-*co*-glycolic acid) (PLGA)) to enable controlled degradation postfunctional completion, reducing long-term biocompatibility risks.

Third, while the closed-loop system effectively integrates neural recording and stimulation, its reliance on external processing hardware limits portability. Miniaturizing the system *via* flexible circuits, low-power wireless modules, and self-powered units (*e.g.*, triboelectric nanogenerators) would facilitate fully implantable, patient-friendly devices.

Finally, exploring the integration of PAACP conductive hydrogel with multifunctional systems that combine electrical stimulation, drug delivery, and tissue repair could expand its clinical applications, especially in personalized medicine. Moreover, miniaturizing the system and incorporating wireless capabilities could enable fully implantable, autonomous devices, making them more suitable for human clinical trials and applications.

CONCLUSION

In this study, we developed a PAACP conductive hydrogel that simultaneously exhibits superior mechanical property, robust bioadhesion, and high conductivity at notably low conductive filler concentration through the collaborative optimization of gel molecular network design, covalent and noncovalent adhesive functional groups, and the distribution of conductive networks. The exceptional mechanical and electrical properties endow the PAACP electrode with significant advantages for both *in vivo* and *in vitro* electrophysiological detection. In electrophysiological applications, PAACP electrodes attached stably and highly conformally to skin texture, improving signal acquisition during movements and achieving higher SNR in sEMG tests compared to commercial gel electrodes. As a cuff electrode, PAACP facilitated suture-free implantation and long-term bidirectional communication with the sciatic nerve. In a closed-loop neuromodulation system for sciatic nerve repair, the PAACP cuff electrode dynamically regulated nerve regeneration through real-time neural activity feedback,

https://doi.org/10.1021/acsnano.5c03336
ACS Nano 2025, 19, 18729–18746

effectively enhancing functional recovery. While further optimization is needed, the hydrogel's facile fabrication, versatile applications, and excellent bioelectronic properties highlight its clinical potential in nerve injury repair and neuromodulation.

EXPERIMENTAL SECTION

Materials. Acrylamide (Sigma-Aldrich, 99%), Acrylic acid (Adamas, 98%), 3-hydroxytyramine hydrochloride (DA·HCl, Adamas, 99%), iron(III) chloride (Sigma-Aldrich, 97%), *N*-succinimidyl methacrylate (Adamas, 98%), *N*,*N*′-methylenebis(acrylamide) (Adamas, 99%), ammonium persulfate (Greagent, 98%), *N*,*N*,*N*′,*N*′-tetramethylethylenediamine (Adamas, 99%). Carboxylated ultrahigh purity single-walled carbon nanotubes (0.15 wt % SWCNTs) were purchased from Nanjing XFNANO Materials Tech Co., Ltd. Commercial cuff electrodes (inner diameter 800 μm), commercial bipolar needle electrode and microelectrode array (MEA) electrode were provided by Kedou (Suzhou) Brain-computer Technology Co., Ltd. Commercial gel electrodes were provided by Intco Medical Technology Co., Ltd. Medical double-sided tape was obtained from Dongxin (Dongguan) Packing Products Co., Ltd. Medical PU film was obtained from Cofoe Medical Technology Co., Ltd.

Animals. Adult male C57BL/6J mice (7 to 8 weeks) were purchased from Charls River Laboratories (n = 24 in total) and were used in *in vivo* biocompatibility (n = 9), *in vivo* stimulation and recording (n = 6) and sciatic nerve injury (n = 9). All animal experiments were conducted under protocols approved by the Institutional Animal Care and Use Committee of the Shanghai Jiao Tong University School of Medicine. Animals were housed under environment with controlled conditions, a 12 h light−dark cycle with food and water provided ad libitum.

Synthesis of PAACP Conductive Hydrogel. First, 15 mg of DA·HCl was dissolved in 1 mL of PBS solution (pH = 7.4) and stirred in an air atmosphere for 15 min to initiate self-polymerization. The dopamine molecules were oxidized and prepolymerized into PDA with the assistance of 4.8 mg of $FeCl_3$, resulting in a brownish precursor solution. Four mL of single-walled carbon nanotube dispersion (0.15 wt %) was added, and PDA was wrapped around the surface of the SWCNTs, modifying the SWCNTs and forming a CNT-PDA solution. Next, 15 mg of AAc-NHS and 0.3 g of AA were mixed thoroughly and allowed to stand for 15 min. Then, 1.5 g of AM and 1 mL of PBS solution were added and mixed thoroughly, followed by the addition of the CNT-PDA solution. Finally, 3 mg of cross-linker MBA, 0.1 g of initiator APS, and 15 μL of initiator accelerator TEMED were added to the mixture. The solution was stirred for 10 min under an ice−water bath. The resulting mixture was poured into a Polytetrafluoroethylene (PTFE) mold and thermally cured at 40 °C for 2 h to obtain the PAACP conductive hydrogel.

Fabrication of PAACP Electrode. The PAACP conductive hydrogel was cut into 1 × 1 cm pieces. The PAACP electrode was connected to the external circuit using conductive copper−nickel tape, and silver paste was applied at the interface between the two to ensure proper electrical contact for the circuit.

Fabrication of PAACP Cuff Electrode. Laser cutting was performed using the DirectLaser SA2 device from Design Comes True Co., Ltd. The electrode was shaped with a front-end width of 0.5 mm (electrode-tissue interface) and a rear-end width of 1 mm (electrode-wire connection). The PAACP cuff electrode was then encapsulated using medical double-sided tape and medical PU film.

Physicochemical Characterization. SEM images were used to characterize the morphology of the hydrogels (SU8200, Hitachi, Japan). Confocal images were employed to examine the morphology of the CNT-PDA solution and the cross-sectional interface between the PAACP conductive hydrogel and different substrates (LEXT OLS5100, Evident, Japan). The molecular structure was analyzed using FT-IR spectroscopy (iN10 iZ10, Thermo Fisher, USA). The distribution of CNT-PDA in the PAACP conductive hydrogel was analyzed by Raman mapping (in Via, Renishaw, UK) and Conductive Atomic Force Microscopy (NTEGRA, NT-MDT, Russia).

Mechanical Characterization. The stress−strain measurements were conducted using a universal testing machine (CMT6103, MTS Systems, China) at a strain rate of 50 mm/min. The tensile adhesive strength was measured using a force gauge (MARK-10, USA), with a moving rate of 500 mm/min. The adhesive strength was calculated as follows

$$P = -\frac{F}{S}$$

where F is the peak force (recorded as a negative value) measured by the force gauge during the test, and S is the contact area between the PAACP conductive hydrogel and the substrate.

Electrochemical Measurement. The resistance variation of the PAACP conductive hydrogel under strain was measured using a True Box RC01 from LinkZill Technology Co., Ltd.. The resistance of the PAACP conductive hydrogel was measured using source measure unit (SMU) instrument (Keithley 2400, USA). and its conductivity was calculated as follows

$$\sigma = \frac{1}{R}\cdot\frac{L}{S}$$

where L is the distance between the two clamps during the measurement, R is the resistance value obtained from the $I-V$ curve measured by the SMU instrument, and S is the cross-sectional area of the conductive hydrogel.

Electrochemical Characterization. The electrochemical properties of the PAACP conductive hydrogel and the skin-electrode contact impedance spectrum were analyzed using an electrochemical workstation (PGSTAT302N, Autolab, Switzerland). To measure the skin-electrode contact impedance, two electrodes were placed on the forearm skin with a 4 cm distance between them. The measurement was conducted with an applied potential of 0.1 V and a frequency window ranging from 0.1 Hz to 10^5 Hz.

The electrochemical properties were measured in a PBS solution using a conventional three-electrode configuration. Prior to testing, the hydrogel was applied to a platinum wire (1 mm diameter) as the working electrode, a counter electrode (1 × 1 cm Pt sheet), and an Ag/AgCl reference electrode were used. Electrochemical impedance spectroscopy (EIS) was performed with an applied potential of 0.1 V and a frequency window ranging from 0.1 Hz to 10^5 Hz. To evaluate the electrochemical stability of the PAACP conductive hydrogel, EIS measurements were also conducted after 1,000 cyclic voltammetry (CV) cycles under the same conditions.

The charge storage capacity (CSC) was measured by CV in the potential range from −0.45 to 1.05 V with a scan rate of 100 mV/s, cycling 1,000 times to evaluate long-term electrochemical stability. The CSC was calculated from the CV data as

$$\mathrm{csc} = \int_{E_2}^{E_1} \frac{i(E)}{2\nu A}\mathrm{d}E$$

Where ν is the scan rate, E_1 and E_2 are the potential window, i is the current at each potential, and A is the area of the electrode.

To measure the charge injection capacity (CIC), biphasic pulses of ±0.5 V with a frequency of 50 Hz were applied, cycling 5,000 times to evaluate long-term electrochemical stability. The CIC was calculated based on the measured output voltage and current using the following formula

$$\mathrm{CIC} = \frac{Q_{\mathrm{inj}(c)} + Q_{\mathrm{inj}(a)}}{A}$$

where $Q_{\mathrm{inj}(c)}$ is the total transferred (or injected) charge in the cathodic phase, $Q_{\mathrm{inj}(a)}$ is the total transferred (or injected) charge in the anodic phase, and A is the area of the electrode.

***In Vitro* sEMG Signals Acquisition.** The surface electromyographic (sEMG) signals were monitored using a wireless electrophysiological signal analysis system (PhysioLAB, INFO Instruments, Germany) at a sampling frequency of 1000 Hz. The sEMG signals were processed using Matlab R2022b and Origin 2018 software. Prior to electrode attachment, the skin was cleaned with alcohol. The signal-to-noise ratio (SNR) was calculated using the following formula

https://doi.org/10.1021/acsnano.5c03336
ACS Nano 2025, 19, 18729−18746

$$\mathrm{SNR} = 20 \times \lg \frac{A_{(s)}}{A_{(n)}}$$

where $A_{(s)}$ represents the RMS value of the signal, and $A_{(n)}$ represents the RMS value of the noise.

***In Vivo* Biocompatibility.** Anesthesia was induced in mice with an intraperitoneal injection of pentobarbital 85 mg/kg body weight (b.w.), the fur on the right hind limb was shaved, and the area was disinfected with iodine. A skin and muscle incision was made to expose the right sciatic nerve for electrode implantation. The electrode lead of the cuff electrode was passed subcutaneously through the back of the mice. In the hydrogel cuff group, the hydrogel cuff was implanted relying on its intrinsic adhesiveness, without the use of sutures. As a positive control, commercial cuff electrodes were implanted and secured with sutures to prevent displacement. The sham surgery group underwent the same surgical procedure but without electrode implantation. *In vivo* biocompatibility analysis was performed 7 days postimplantation. The sciatic nerve were meticulously dissected from surrounding muscle tissues, and the implanted electrodes carefully removed. The obtained nerve tissues underwent fixation with 4% paraformaldehyde, dehydration, and embedding with optimal cutting temperature compound (Absin Bioscience Inc., China). Then the nerve segments encapsulated by the electrodes were sectioned and stained for further analysis. NF200 (1:100, Invitrogen, SIGMA-Aldrich, USA), S-100 (1:200, Servicebio, China), and Iba-1 (1:500, Servicebio, China) were selected as markers for immunofluorescence staining to assess cell viability and inflammatory responses. DAPI was used to stain cell nuclei. ImageJ software was employed for analyzing biomarker fluorescence intensity.

***In Vivo* Stimulation and Recording.** The implantation procedure was performed as described in previous experiments. After anesthesia, PAACP cuff electrodes were implanted in the mice, and biphasic charge-balanced rectangular voltage pulses (0.5 Hz, 0.5−6 V, 1 ms pulse width) were applied using a Pulse Stimulator (Master-9, AMPI, Israel). The angle changes of the ankle joint were processed using ImageJ software. *In vivo* compound nerve action potentials (CNAPs) and compound muscle action potentials (CMAPs) were monitored using a 64-channel neural workstation (Apollo II, Bio-Signal Technologies, China), and the signals were analyzed using Matlab R2022b and Origin 2018 software.

Microelectrode Array Implantation. The mice were deeply anesthetized with intraperitoneal injection of a 85 mg/kg body weight (b.w.) pentobarbital. The top of the head was shaved, cleaned with 75% ethanol, and then positioned in the stereotactic frame. Ophthalmic ointment was applied, the skin above skull was removed and small craniotomy was performed using a drill to open a 1 mm × 1 mm window above the left M1 [anterior-posterior (AP): −0.5 mm, medial-lateral (ML): 0.8 mm, dorsal-ventral (DV): 0.7 mm from dura,]. a 4 × 4 microelectrode array (Kedou (Suzhou) Brain-computer Technology Co, China) was slowly lowered to the aimed depth. Dental cement then was applied to secure the electrode to the skull.

Sciatic Nerve Injury Model. Nine mice were randomly divided into three groups: closed-loop (CL) stimulation paradigm, random (RD) stimulation paradigm, and control. Prior to creating the injury model, a microelectrode array (MEA) electrode was implanted in the M1 region of the mice brain as described above, followed by a recovery period of 2 days. During surgery, as described in the previous experiment, the right sciatic nerve was exposed. In the SNI + CL and SNI + RD groups, a crushing injury was induced at the bifurcation of the sciatic nerve by placing a hemostat across the nerve and applying firm pressure for 10 s three times. The injured site was then wrapped with PAACP conductive hydrogel, and a PAACP cuff electrode was implanted. No additional treatment was applied to the control group. All mice were allowed to recover and were regularly monitored for any changes. Euthanasia was performed at specified time points, and the nerves and muscles were collected for subsequent analysis.

Closed-Loop Regulation System. Local field potential (LFP) signals were acquired using a multichannel neural electrophysiological system (alphaRS, AlphaOmega, Israel). LFP signals processing was performed using Matlab R2022b software. Biphasic charge-balanced rectangular voltage pulses (20 Hz, 1.25 V, 0.1 ms pulse width) were applied using a Pulse Stimulator (Master-8, AMPI, Israel). Mice received either CL or RD treatment daily from days 3−14 postinjury, with each treatment session lasting 15 min. In the SNI + CL group, mice were awake and placed on a grid platform for CL treatment, while in the SNI + RD group, mice were anesthetized during RD treatment.

Cortically Evoked EMG Signals Acquisition. We evaluated functional recovery before and every week after SNI. The mice were anesthetized with isoflurane and stabilized in the stereotactic frame. The stimulation involving a train of 15 bipolar pulses at 50 Hz in 1 ms durations at 2 mA was delivered through the microelectrode implanted in M1 using the multichannel neural electrophysiological system (alphaRS, AlphaOmega, Israel). Every channel in the 4 × 4 microelectrode array was tested before EMG signal acquisition, and the channel elicited the strongest EMG response was selected and used though out the experiment. The right hindlimb was shaved and a bipolar stainless steel needle (tip distance, 1 mm) was inserted into the biceps muscles. and the reactions to stimulation were recorded with a 64-channel neural workstation (Apollo II, Bio-Signal Technologies, China) at 30,000 Hz. Action potential is defined as the arithmetic mean of ten stimulations.

Tissue Processing and Immunohistochemistry. After the hindlimb function was tested, the mice were deeply anesthetized with intraperitoneal injection of a 85 mg/kg b.w. pentobarbital and transcardially perfused with a solution of 4% paraformaldehyde in 0.1 M PB (phosphate buffer). The gastrocnemius muscle muscles were carefully dissected from the hindlimbs and weighted. The muscles then were postfixed in 4% paraformaldehyde in 0.1 M PB for 24 h and dehydrated in 30% sucrose in 0.1 M PB for 48 h. The tissues were then embedded in optimal cutting temperature compound (Absin Bioscience Inc., China) and frozen at −20 °C. The tissues were stored at −80 °C until further analysis.

Muscle sections at every 40 μm were used for quantification. Sections from each experimental group were stained with α-BTX recognized as α-subunit of AChR of NMJ and NF-200 antibody recognized as neural fiber. After treatment with 10% normal donkey serum (Abbkine Inc., China) in 0.1% Triton X-100 for 2 h at room temperature, the muscle sections were incubated with α-BTX conjugated with Alexa Fluor 647 (1:500, Invitrogen, Thermo Fisher Scientific Inc., USA) for 2 h at room temperature and rabbit polyclonal anti-NF-200 (1:100, Invitrogen, SIGMA-Aldrich, USA) for 24 h at 4 °C. The NF-200 antibody was visualized with Alexa Fluor 555 donkey antirabbit IgG (H + L) (1:500, Invitrogen, Thermo Fisher Scientific Inc., USA) for 2 h at room temperature. Images were obtained on an FV3000 Olympus microscope (Olympus Optical Co., Ltd., Tokyo, Japan).

Quantitative Analyses of NMJs. To evaluate AChR distribution and innervation, sections sampled every 40 μm were stained with α-BTX and NF-200, and images were obtained using an FV3000 Olympus microscope with 40× magnification. We first evaluated the innervation of α-BTX-positive clusters, which was defined to receive none, partial or full innervation of axons according to the colocalization of α-BTX and NF-200. The positive clusters were counted with regard to the innervation type and The ratio of each type to the total number of α-BTX-positive clusters was calculated. We also evaluated the morphology of α-BTX-positive clusters, which was divided into three types: "pretzel" (mature, with a weblike pattern including multiple perforations), "plaque" (immature and smaller size lacking perforations), and "intermediate" (between plaque and pretzel morphology). The positive clusters were counted with regard to the morphology type. The ratio of each type to the total number of α-BTX-positive clusters was calculated to provide a morphological index for NMJs.

Statistical Analysis. Statistical analysis was performed using GraphPad software. All experiments were conducted with at least three replicates ($n \geq 3$) for each sample. For statistical analysis of multiple samples, one-way analysis of variance (ANOVA) was initially used, followed by Tukey's multiple comparison test. Data are presented as the mean ± standard deviation. Significance levels are indicated as * for $p \leq 0.05$, ** for $p \leq 0.01$, *** for $p \leq 0.001$, and NS for not significant.

https://doi.org/10.1021/acsnano.5c03336
ACS Nano 2025, 19, 18729−18746

ASSOCIATED CONTENT

Supporting Information

The Supporting Information is available free of charge at https://pubs.acs.org/doi/10.1021/acsnano.5c03336.

Figures S1−S13: Confocal microscope images of CNT and CNT-PDA; tensile stress−strain test and SEM image; photograph of $PAA_{0.2}C_{0.006}P_{0.15}$ conductive hydrogel when stretched 300% on Ecoflex elastomer; Adhesion performances of PAACP conductive hydrogels; photograph of PAAC conductive hydrogel and PAACP conductive hydrogel (conductive filler content 0.33 wt %); photographs of PAACP conductive hydrogels; photographs of PAAC conductive hydrogels; biocompatibility of PAACP conductive hydrogels; Raman spectra and $\Delta R/R_0$ of PAACP conductive hydrogels; skin-electrode interface impedance test; photographs related to sEMG test; stimulating and recording *in vivo*; photographs of the actual setup *in vivo* stimulation and recording experiment. Table S1−S4: reagent dosage table for hydrogels of different ratios; modulus and elongation at break of hydrogels of different ratios; comparison of CSC and CIC values for electrodes used in electrophysiological monitoring; resistance of PAACP and PAAC conductive hydrogels (PDF)

Movie S1: PAACP conductive hydrogel lifts 500 g weights after being immersed in water for 1 day (AVI)

Movie S2: PAACP cuff electrode implantation into sciatic nerve of mice (AVI)

Movie S3: Closed-loop stimulation system decodes movement intentions in real-time by LFP signals (AVI)

AUTHOR INFORMATION

Corresponding Authors

Zhengrun Gao − *Department of Neurology, Songjiang Research Institute, Shanghai Key Laboratory of Emotions and Affective Disorders, Songjiang Hospital Affiliated to Shanghai Jiao Tong University, School of Medicine, Shanghai 201600, China*; Email: zrgao@shsmu.edu.cn

Ranran Wang − *State Key Laboratory of High Performance Ceramics and Superfine Microstructure, Shanghai Institute of Ceramics, Chinese Academy of Sciences, Shanghai 200050, China; School of Chemistry and Materials Science, Hangzhou Institute for Advanced Study, University of Chinese Academy of Sciences, Hangzhou 310024, China*; orcid.org/0000-0001-5097-2834; Email: wangranran@mail.sic.ac.cn

Authors

Tianfei Chu − *State Key Laboratory of High Performance Ceramics and Superfine Microstructure, Shanghai Institute of Ceramics, Chinese Academy of Sciences, Shanghai 200050, China; Center of Materials Science and Optoelectronics Engineering, University of Chinese Academy of Sciences, Beijing 100049, China*

Yuanjie Xiao − *Department of Neurology, Songjiang Research Institute, Shanghai Key Laboratory of Emotions and Affective Disorders, Songjiang Hospital Affiliated to Shanghai Jiao Tong University, School of Medicine, Shanghai 201600, China*

Huiting Lai − *State Key Laboratory of High Performance Ceramics and Superfine Microstructure, Shanghai Institute of Ceramics, Chinese Academy of Sciences, Shanghai 200050, China; Center of Materials Science and Optoelectronics Engineering, University of Chinese Academy of Sciences, Beijing 100049, China*

Liangjing Shi − *State Key Laboratory of High Performance Ceramics and Superfine Microstructure, Shanghai Institute of Ceramics, Chinese Academy of Sciences, Shanghai 200050, China*

Yin Cheng − *State Key Laboratory of High Performance Ceramics and Superfine Microstructure, Shanghai Institute of Ceramics, Chinese Academy of Sciences, Shanghai 200050, China*; orcid.org/0000-0001-7647-3558

Jing Sun − *State Key Laboratory of High Performance Ceramics and Superfine Microstructure, Shanghai Institute of Ceramics, Chinese Academy of Sciences, Shanghai 200050, China*; orcid.org/0000-0003-1101-1584

Zhen Pang − *Department of Neurology, Songjiang Research Institute, Shanghai Key Laboratory of Emotions and Affective Disorders, Songjiang Hospital Affiliated to Shanghai Jiao Tong University, School of Medicine, Shanghai 201600, China*

Shihui Cheng − *Department of Neurology, Songjiang Research Institute, Shanghai Key Laboratory of Emotions and Affective Disorders, Songjiang Hospital Affiliated to Shanghai Jiao Tong University, School of Medicine, Shanghai 201600, China*

Kunkun Zhao − *Modern Research Center for Traditional Chinese Medicine, Shanxi University, Taiyuan 030006, China*

Complete contact information is available at: https://pubs.acs.org/10.1021/acsnano.5c03336

Author Contributions

#T.C. and Y.X. contributed equally to this work.

Notes

The authors declare no competing financial interest.

ACKNOWLEDGMENTS

This work was financially supported by the National Key Research and Development Program of China (Grant No. 2024YFB3814100), the National Natural Science Foundation of China (Grant Nos. U24A20228, 62261136551, 62301540), the Chinese Academy of Sciences Project for Young Scientists in Basic Research (Grant No.YSBR-109), and the Natural Science Foundation of Shanghai (Grant No. 22ZR1481700). The TOC graphic, Figures 5c and 6a,b were created with BioRender.com under an Academic Publication License.

REFERENCES

(1) El Seblani, N.; Welleford, A. S.; Quintero, J. E.; van Horne, C. G.; Gerhardt, G. A. Invited review: Utilizing peripheral nerve regenerative elements to repair damage in the CNS. *J. Neurosci. Methods* **2020**, *335*, 108623.

(2) Zhou, W. J. L.; Jiang, Y. W.; Xu, Q.; Chen, L. P.; Qiao, H.; Wang, Y. X.; Lai, J. C.; Zhong, D. L.; Zhang, Y.; Li, W. N.; et al. Soft and stretchable organic bioelectronics for continuous intraoperative neurophysiological monitoring during microsurgery. *Nat. Biomed. Eng.* **2023**, *7* (10), 1270−1281.

(3) Hong, J. W.; Yoon, C.; Jo, K.; Won, J. H.; Park, S. Recent advances in recording and modulation technologies for next-generation neural interfaces. *Iscience* **2021**, *24* (12), 103550.

(4) Song, E. M.; Li, J. H.; Won, S. M.; Bai, W. B.; Rogers, J. A. Materials for flexible bioelectronic systems as chronic neural interfaces. *Nat. Mater.* **2020**, *19* (6), 590−603.

(5) Yang, M.; Wang, L. F.; Liu, W. L.; Li, W. L.; Huang, Y. W.; Jin, Q. F.; Zhang, L.; Jiang, Y. W.; Luo, Z. Q. Highly-stable, injectable, conductive hydrogel for chronic neuromodulation. *Nat. Commun.* **2024**, *15* (1), 7993.

(6) Terutsuki, D.; Yoroizuka, H.; Osawa, S.; Ogihara, Y.; Abe, H.; Nakagawa, A.; Iwasaki, M.; Nishizawa, M. Totally Organic Hydrogel-Based Self-Closing Cuff Electrode for Vagus Nerve Stimulation. *Adv. Healthcare Mater.* **2022**, *11* (23), 2201627.
(7) Topalovic, U.; Barclay, S.; Ling, C. K.; Alzuhair, A.; Yu, W. H.; Hokhikyan, V.; Chandrakumar, H.; Rozgic, D.; Jiang, W. L.; Basir-Kazeruni, S.; et al. A wearable platform for closed-loop stimulation and recording of single-neuron and local field potential activity in freely moving humans. *Nat. Neurosci.* **2023**, *26* (3), 517−527.
(8) Oh, S.; Jekal, J.; Liu, J.; Kim, J.; Park, J. U.; Lee, T. Y.; Jang, K. I. Bioelectronic Implantable Devices for Physiological Signal Recording and Closed-Loop Neuromodulation. *Adv. Funct. Mater.* **2024**, *34* (41), 2403562.
(9) Larson, C. E.; Meng, E. A review for the peripheral nerve interface designer. *J. Neurosci. Methods* **2020**, *332*, 108523.
(10) Lacour, S. P.; Courtine, G.; Guck, J. Materials and technologies for soft implantable neuroprostheses. *Nat. Rev. Mater.* **2016**, *1* (10), 16063.
(11) Lee, Y. J.; Kim, H. J.; Do, S. H.; Kang, J. Y.; Lee, S. H. Characterization of nerve-cuff electrode interface for biocompatible and chronic stimulating application. *Sens. Actuators, B* **2016**, *237*, 924−934.
(12) Cuttaz, E. A.; Bailey, Z. K.; Chapman, C. A. R.; Goding, J. A.; Green, R. A. Polymer Bioelectronics: A Solution for Both Stimulating and Recording Electrodes. *Adv. Healthcare Mater.* **2024**, *13* (24), 2304447.
(13) Lienemann, S.; Zötterman, J.; Farnebo, S.; Tybrandt, K. Stretchable gold nanowire-based cuff electrodes for low-voltage peripheral nerve stimulation. *J. Neural Eng.* **2021**, *18* (4), 045007.
(14) Heo, D. N.; Kim, H.-J.; Lee, Y. J.; Heo, M.; Lee, S. J.; Lee, D.; Do, S. H.; Lee, S. H.; Kwon, I. K. Flexible and Highly Biocompatible Nanofiber-Based Electrodes for Neural Surface Interfacing. *ACS Nano* **2017**, *11* (3), 2961−2971.
(15) Xiang, Z.; Yen, S. C.; Sheshadri, S.; Wang, J.; Lee, S.; Liu, Y. H.; Liao, L. D.; Thakor, N. V.; Lee, C. Progress of Flexible Electronics in Neural Interfacing - A Self-Adaptive Non-Invasive Neural Ribbon Electrode for Small Nerves Recording. *Adv. Mater.* **2016**, *28* (22), 4472−4479.
(16) Wang, X. Q.; Chan, K. H.; Lu, W. H.; Ding, T. P.; Ng, S. W. L.; Cheng, Y.; Li, T. T.; Hong, M. H.; Tee, B. C. K.; Ho, G. W. Macromolecule conformational shaping for extreme mechanical programming of polymorphic hydrogel fibers. *Nat. Commun.* **2022**, *13* (1), 3369.
(17) Cao, P. L.; Wang, Y.; Yang, J.; Niu, S. C.; Pan, X. L.; Lu, W. H.; Li, L. H.; Xu, Y. M.; Cui, J. B.; Ho, G. W.; et al. Scalable Layered Heterogeneous Hydrogel Fibers with Strain-Induced Crystallization for Tough, Resilient, and Highly Conductive Soft Bioelectronics. *Adv. Mater.* **2024**, *36* (48), 2409632.
(18) Ara, L.; Khan, M.; Ullah, R.; Shah, L. A. Hydrophobically associated ionic conductive hydrogels as strain, pressure, and an electronic sensor for human motions detection. *Sens. Actuators, A* **2023**, *362*, 114618.
(19) Khan, M.; Shah, L. A.; Ara, L.; Ullah, R.; Yoo, H. M. Micelle-Micelle Cross-Linked Highly Stretchable Conductive Hydrogels for Potential Applications of Strain and Electronic Skin Sensors. *Chem. Mater.* **2023**, *35* (14), 5582−5592.
(20) Khan, M.; Rahman, T. U.; Sher, M.; Shah, L. A.; Md Akil, H.; Fu, J.; Yoo, H. M. Flexible Ionic Conductive Hydrogels with Wrinkled Texture for Flexible Strain Transducer with Language Identifying Diversity. *Chem. Mater.* **2024**, *36* (9), 4703−4713.
(21) Khan, M.; Shah, L. A.; Rahman, T. U.; Ara, L.; Yoo, H. M. Multiple-Language-Responsive Conductive Hydrogel Composites for Flexible Strain and Epidermis Sensors. *ACS Appl. Polym. Mater.* **2024**, *6* (7), 4233−4243.
(22) Hifsa, H.; Khan, M.; Ara, L.; Shah, L. A.; Md Akil, H.; Fu, J. Multifunctional Capabilities of Malonic Acid-Bridged Conductive Hydrogels for Wearable Electronic Devices. *ACS Appl. Polym. Mater.* **2024**, *6* (16), 9940−9951.
(23) Liu, X. Y.; Liu, J.; Lin, S. T.; Zhao, X. H. Hydrogel machines. *Mater. Today* **2020**, *36*, 102−124.
(24) Zhang, Y.; Tan, Y.; Lao, J.; Gao, H.; Yu, J. Hydrogels for Flexible Electronics. *ACS Nano* **2023**, *17* (11), 9681−9693.
(25) Won, D.; Kim, H.; Kim, J.; Kim, H.; Kim, M. W.; Ahn, J.; Min, K. J.; Lee, Y. S.; Hong, S. K.; Choi, J.; et al. Laser-induced wet stability and adhesion of pure conducting polymer hydrogels. *Nat. Electron.* **2024**, *7* (6), 475−486.
(26) Zhou, T.; Yuk, H.; Hu, F. Q.; Wu, J. J.; Tian, F. J.; Roh, H.; Shen, Z. Q.; Gu, G. Y.; Xu, J. K.; Lu, B. Y.; et al. 3D printable high-performance conducting polymer hydrogel for all-hydrogel bioelectronic interfaces. *Nat. Mater.* **2023**, *22* (7), 895−902.
(27) Won, D.; Kim, J.; Choi, J.; Kim, H.; Han, S.; Ha, I.; Bang, J.; Kim, K. K.; Lee, Y.; Kim, T. S.; et al. Digital selective transformation and patterning of highly conductive hydrogel bioelectronics by laser-induced phase separation. *Sci. Adv.* **2022**, *8* (23), No. eabo3209.
(28) Yu, M.; Wang, C. X.; Cui, H. Q.; Huang, J. P.; Yu, Q. H. Y.; Wang, P.; Huang, C.; Li, G. L.; Zhao, Y.; Du, X. M.; et al. Self-Closing Stretchable Cuff Electrodes for Peripheral Nerve Stimulation and Electromyographic Signal Recording. *ACS Appl. Mater. Interfaces* **2023**, *15* (6), 7663−7672.
(29) He, J. H.; Shi, M. T.; Liang, Y. P.; Guo, B. L. Conductive adhesive self-healing nanocomposite hydrogel wound dressing for photothermal therapy of infected full-thickness skin wounds. *Chem. Eng. J.* **2020**, *394*, 124888.
(30) Li, N.; Wang, X. L.; Liu, Y.; Li, Y. F.; Li, J. S.; Qin, Z. H.; Jiao, T. F. Ultrastretchable, Self-Adhesive and conductive MXene nanocomposite hydrogel for body-surface temperature distinguishing and electrophysiological signal monitoring. *Chem. Eng. J.* **2024**, *483*, 149303.
(31) Yu, C. J.; Shi, M.; He, S. S.; Yao, M. M.; Sun, H.; Yue, Z. W.; Qiu, Y. W.; Liu, B. J.; Liang, L.; Zhao, Z. M.; et al. Chronological adhesive cardiac patch for synchronous mechanophysiological monitoring and electrocoupling therapy. *Nat. Commun.* **2023**, *14* (1), 6226.
(32) Zhao, Y. S.; Zhang, B. Z.; Yao, B. W.; Qiu, Y.; Peng, Z. H.; Zhang, Y. C.; Alsaid, Y.; Frenkel, I.; Youssef, K.; Pei, Q. B.; et al. Hierarchically Structured Stretchable Conductive Hydrogels for High-Performance Wearable Strain Sensors and Supercapacitors. *Matter* **2020**, *3* (4), 1196−1210.
(33) Han, L.; Liu, K. Z.; Wang, M. H.; Wang, K. F.; Fang, L. M.; Chen, H. T.; Zhou, J.; Lu, X. Mussel-Inspired Adhesive and Conductive Hydrogel with Long-Lasting Moisture and Extreme Temperature Tolerance. *Adv. Funct. Mater.* **2018**, *28* (3), 1704195.
(34) Sennakesavan, G.; Mostakhdemin, M.; Dkhar, L. K.; Seyfoddin, A.; Fatihhi, S. J. Acrylic acid/acrylamide based hydrogels and its properties - A review. *Polym. Degrad. Stab.* **2020**, *180*, 109308.
(35) Wang, Z. W.; Wei, H.; Huang, Y. J.; Wei, Y.; Chen, J. Naturally sourced hydrogels: emerging fundamental materials for next-generation healthcare sensing. *Chem. Soc. Rev.* **2023**, *52* (9), 2992−3034.
(36) Hou, Y.; Li, Y.; Li, Y.; Li, D.; Guo, T.; Deng, X.; Zhang, H.; Xie, C.; Lu, X. Tuning Water-Resistant Networks in Mussel-Inspired Hydrogels for Robust Wet Tissue and Bioelectronic Adhesion. *ACS Nano* **2023**, *17* (3), 2745−2760.
(37) Chen, X. Y.; Yuk, H.; Wu, J. J.; Nabzdyk, C. S.; Zhao, X. H. Instant tough bioadhesive with triggerable benign detachment. *Proc. Natl. Acad. Sci. U.S.A.* **2020**, *117* (27), 15497−15503.
(38) Han, L.; Yan, L. W.; Wang, M. H.; Wang, K. F.; Fang, L. M.; Zhou, J.; Fang, J.; Ren, F. Z.; Lu, X. Transparent, Adhesive, and Conductive Hydrogel for Soft Bioelectronics Based on Light-Transmitting Polydopamine-Doped Polypyrrole Nanofibrils. *Chem. Mater.* **2018**, *30* (16), 5561−5572.
(39) Xing, L.; Song, Y. T.; Zou, X. Q.; Tan, H. J.; Yan, J. N.; Wang, J. K. A mussel-inspired semi-interpenetrating structure hydrogel with superior stretchability, self-adhesive properties, and pH sensitivity for smart wearable electronics. *J. Mater. Chem. C* **2023**, *11* (39), 13376−13386.
(40) Han, L.; Lu, X.; Wang, M.; Gan, D.; Deng, W.; Wang, K.; Fang, L.; Liu, K.; Chan, C. W.; Tang, Y.; et al. A Mussel-Inspired Conductive, Self-Adhesive, and Self-Healable Tough Hydrogel as Cell Stimulators and Implantable Bioelectronics. *Small* **2017**, *13* (2), 1601916.

https://doi.org/10.1021/acsnano.5c03336
ACS Nano 2025, 19, 18729−18746

(41) Yu, G. F.; Zhang, Y.; Wang, Q.; Dan, N. H.; Chen, Y. N.; Li, Z. J.; Dan, W. H.; Wang, Y. B. Wearable and Flexible Hydrogels for Strain Sensing and Wound Electrical Stimulation. *Ind. Eng. Chem. Res.* **2023**, *62* (13), 5468−5481.
(42) Qin, Z.; Pugno, N. M.; Buehler, M. J. Mechanics of fragmentation of crocodile skin and other thin films. *Sci. Rep.* **2014**, *4* (1), 4966.
(43) Sun, J. Y.; Zhao, X. H.; Illeperuma, W. R. K.; Chaudhuri, O.; Oh, K. H.; Mooney, D. J.; Vlassak, J. J.; Suo, Z. G. Highly stretchable and tough hydrogels. *Nature* **2012**, *489* (7414), 133−136.
(44) Lv, Y. C.; Cai, F. Y.; He, Y. X.; Li, L.; Huang, Y. F.; Yang, J. M.; Zheng, Y. Q.; Shi, X. A. Multi-crosslinked hydrogels with strong wet adhesion, self-healing, antibacterial property, reactive oxygen species scavenging activity, and on-demand removability for seawater-immersed wound healing. *Acta Biomater.* **2023**, *159*, 95−110.
(45) Xue, B.; Gu, J.; Li, L.; Yu, W. T.; Yin, S.; Qin, M.; Jiang, Q.; Wang, W.; Cao, Y. Hydrogel tapes for fault-tolerant strong wet adhesion. *Nat. Commun.* **2021**, *12* (1), 7156.
(46) Wu, J. J.; Yuk, H.; Sarrafian, T. L.; Guo, C. F.; Griffiths, L. G.; Nabzdyk, C. S.; Zhao, X. H. An off-the-shelf bioadhesive patch for sutureless repair of gastrointestinal defects. *Sci. Transl. Med.* **2022**, *14* (630), No. eabh2857.
(47) Zhang, C.; Wu, B. H.; Zhou, Y. S.; Zhou, F.; Liu, W. M.; Wang, Z. K. Mussel-inspired hydrogels: from design principles to promising applications. *Chem. Soc. Rev.* **2020**, *49* (11), 3605−3637.
(48) Zhang, R.; Yang, A.; Yang, Y. T.; Zhu, Y. C.; Song, Y. M.; Li, Y.; Li, J. Mussel-inspired cellulose nanofiber/poly(vinyl alcohol) hydrogels with robustness, self-adhesion and antimicrobial activity for strain sensors. *Int. J. Biol. Macromol.* **2023**, *245*, 125469.
(49) Chen, C. C.; Wang, Y. R.; Meng, T. T.; Wu, Q. J.; Fang, L.; Zhao, D.; Zhang, Y. Y.; Li, D. G. Electrically conductive polyacrylamide/carbon nanotube hydrogel: reinforcing effect from cellulose nanofibers. *Cellulose* **2019**, *26* (16), 8843−8851.
(50) Sun, X.; Qin, Z. H.; Ye, L.; Zhang, H. T.; Yu, Q. Y.; Wu, X. J.; Li, J. J.; Yao, F. L. Carbon nanotubes reinforced hydrogel as flexible strain sensor with high stretchability and mechanically toughness. *Chem. Eng. J.* **2020**, *382*, 122832.
(51) Qin, Z. H.; Sun, X.; Yu, Q. Y.; Zhang, H. T.; Wu, X. J.; Yao, M. M.; Liu, W. W.; Yao, F. L.; Li, J. J. Carbon Nanotubes/Hydrophobically Associated Hydrogels as Ultrastretchable, Highly Sensitive, Stable Strain, and Pressure Sensors. *ACS Appl. Mater. Interfaces* **2020**, *12* (4), 4944−4953.
(52) Quan, Q. Y.; Zhao, T. Y.; Luo, Z.; Li, B. X.; Sun, H.; Zhao, H. Y.; Yu, Z. Z.; Yang, D. Z. Antifreezing, Antidrying, and Conductive Hydrogels for Electronic Skin Applications at Ultralow Temperatures. *ACS Appl. Mater. Interfaces* **2024**, *16* (16), 21133−21145.
(53) Yin, H. Y.; Chen, L. Z.; Liu, F. F.; Abdiryim, T.; Chen, J. Y.; Jing, X. Y.; Li, Y. C.; Su, M. Y.; Liu, X. MXene-based conductive hydrogels with toughness and self-healing enhancement by metal coordination for flexible electronic devices. *Mater. Today Phys.* **2024**, *47*, 101537.
(54) Li, S.-N.; Yu, Z.-R.; Guo, B.-F.; Guo, K.-Y.; Li, Y.; Gong, L.-X.; Zhao, L.; Bae, J.; Tang, L.-C. Environmentally stable, mechanically flexible, self-adhesive, and electrically conductive Ti3C2TX MXene hydrogels for wide-temperature strain sensing. *Nano Energy* **2021**, *90*, 106502.
(55) Ni, Q. Y.; He, X. F.; Zhou, J. L.; Yang, Y. Q.; Zeng, Z. F.; Mao, P. F.; Luo, Y. H.; Xu, J. M.; Jiang, B. Y.; Wu, Q.; et al. Mechanical tough and stretchable quaternized cellulose nanofibrils/MXene conductive hydrogel for flexible strain sensor with multi-scale monitoring. *J. Mater. Sci. Technol.* **2024**, *191*, 181−191.
(56) Du, P.; Wang, J.; Hsu, Y.; Uyama, H. Bio-Inspired Homogeneous Conductive Hydrogel with Flexibility and Adhesiveness for Information Transmission and Sign Language Recognition. *ACS Appl. Mater. Interfaces* **2023**, *15* (19), 23711−23724.
(57) Shi, M. T.; Dong, R. A.; Hu, J.; Guo, B. L. Conductive self-healing biodegradable hydrogel based on hyaluronic acid-grafted-polyaniline as cell recruitment niches and cell delivery carrier for myogenic differentiation and skeletal muscle regeneration. *Chem. Eng. J.* **2023**, *457*, 141110.
(58) Peng, Y.; Yan, B.; Li, Y.; Lan, J.; Shi, L.; Ran, R. Antifreeze and moisturizing high conductivity PEDOT/PVA hydrogels for wearable motion sensor. *J. Mater. Sci.* **2020**, *55* (3), 1280−1291.
(59) Wang, F.; Xue, Y.; Chen, X.; Zhang, P.; Shan, L.; Duan, Q.; Xing, J.; Lan, Y.; Lu, B.; Liu, J. 3D Printed Implantable Hydrogel Bioelectronics for Electrophysiological Monitoring and Electrical Modulation. *Adv. Funct. Mater.* **2024**, *34* (21), 2314471.
(60) Wan, R. T.; Yu, J. W.; Quan, Z. Y.; Ma, H. D.; Li, J. H.; Tian, F. J.; Wang, W.; Sun, Y. J.; Liu, J. Y.; Gao, D.; et al. A reusable, healable, and biocompatible PEDOT:PSS hydrogel-based electrical bioadhesive interface for high-resolution electromyography monitoring and time-frequency analysis. *Chem. Eng. J.* **2024**, *490*, 151454.
(61) Zhang, M.; Wang, Y. X.; Liu, K.; Liu, Y.; Xu, T.; Du, H. S.; Si, C. L. Strong, conductive, and freezing-tolerant polyacrylamide/PEDOT:PSS/cellulose nanofibrils hydrogels for wearable strain sensors. *Carbohydr. Polym.* **2023**, *305*, 120567.
(62) Lu, B. Y.; Yuk, H.; Lin, S. T.; Jian, N. N.; Qu, K.; Xu, J. K.; Zhao, X. H. Pure PEDOT:PSS hydrogels. *Nat. Commun.* **2019**, *10* (1), 1043.
(63) Tian, G. W.; Yang, D.; Liang, C. Y.; Liu, Y.; Chen, J. H.; Zhao, Q. Y.; Tang, S. L.; Huang, J. P.; Xu, P.; Liu, Z. Y.; et al. A Nonswelling Hydrogel with Regenerable High Wet Tissue Adhesion for Bioelectronics. *Adv. Mater.* **2023**, *35* (18), 2212302.
(64) Yuk, H.; Lu, B.; Zhao, X. Hydrogel bioelectronics. *Chem. Soc. Rev.* **2019**, *48* (6), 1642−1667.
(65) Zhang, Y. C.; Zheng, N.; Cao, Y.; Wang, F. L.; Wang, P.; Ma, Y. J.; Lu, B. W.; Hou, G. H.; Fang, Z. Z.; Liang, Z. W.; et al. Climbing-inspired twining electrodes using shape memory for peripheral nerve stimulation and recording. *Sci. Adv.* **2019**, *5* (4), No. eaaw1066.
(66) Wang, C. R.; Shirzaei Sani, E.; Shih, C. D.; Lim, C. T.; Wang, J.; Armstrong, D. G.; Gao, W. Wound management materials and technologies from bench to bedside and beyond. *Nat. Rev. Mater.* **2024**, *9* (8), 550−566.
(67) Kong, J. J.; Teng, C.; Liu, F. L.; Wang, X. Z. Y.; Zhou, Y.; Zong, Y.; Wan, Z. X.; Qin, J.; Yu, B.; Mi, D. G.; et al. Enhancing regeneration and repair of long-distance peripheral nerve defect injuries with continuous microcurrent electrical nerve stimulation. *Front. Neurosci.* **2024**, *18*, 1361590.
(68) Liu, Z. H.; Liu, Y. S.; Yushan, M.; Yusufu, A. Enhanced Nerve Regeneration by Bionic Conductive Nerve Scaffold Under Electrical Stimulation. *Front. Neurosci.* **2022**, *16*, 810676.
(69) Li, X.; Zhang, T.; Li, C.; Xu, W.; Guan, Y.; Li, X.; Cheng, H.; Chen, S.; Yang, B.; Liu, Y.; et al. Electrical stimulation accelerates Wallerian degeneration and promotes nerve regeneration after sciatic nerve injury. *Glia* **2023**, *71* (3), 758−774.
(70) Samejima, S.; Khorasani, A.; Ranganathan, V.; Nakahara, J.; Tolley, N. M.; Boissenin, A.; Shalchyan, V.; Daliri, M. R.; Smith, J. R.; Moritz, C. T. Brain-Computer-Spinal Interface Restores Upper Limb Function After Spinal Cord Injury. *IEEE Trans. Neural Syst. Rehabil. Eng.* **2021**, *29*, 1233−1242.

https://doi.org/10.1021/acsnano.5c03336
ACS Nano 2025, 19, 18729−18746